PIEZO-PHOTOTRONIC EFFECT IN

2D III-VI COMPOUND BASED

HETEROSTRUCTURES FOR

OPTOELECTRONIC DEVICE

APPLICATIONS

ZHAO Yuqian

MPhil

The Hong Kong Polytechnic University

2021

The Hong Kong Polytechnic University

Department of Applied Physics

Piezo-phototronic effect in 2D III-VI compound based heterostructures for optoelectronic device applications

ZHAO Yuqian

A thesis submitted in partial fulfillment of the requirements for the degree of Master of Philosophy

August 2021

CERTIFICATE OF ORIGINALITY

I hereby declare that this thesis is my own work and that, to the best of my knowledge and belief, it reproduces no material previously published or written, nor material that has been accepted for the award of any other degree or diploma, except where due acknowledgement has been made in the text.

_____(Signed)

_____ZHAO Yuqian_____(Name of student)

Abstract

The piezo-phototronic effect is known as a three-way coupling among photoexcitation, piezoelectric and semiconducting properties, which attracts significant attention owing to the potential modulation to the generation, transportation, separation and recombination of the photo-excited charge carriers near the metal-semiconductor Schottky contact and p-n junction by the strain-induced piezo-potential.

Comparing to the rest of heterojunctions, p-n junction has been broadly investigated as it plays a vital role for numerous modern commercial optoelectronics through the beneficial characteristic combination of each material to enhance the device performance. In contrast to one-dimensional (1D) and three-dimensional (3D) materials, two-dimensional (2D) materials present various advantages involving distinctive and simple crystal morphology, adjustable energy band gaps and the absence of traditional consideration of lattice mismatch during contact, beneficial for building up van der Waals (vdW) heterostructures in multiple applications. Besides, photoelectric conversion becomes more efficient in 2D crystals as the recombination of carriers has been largely suppressed with a reduction of the interface defects. Although p-n junction based on 2D materials have remarkable ductility and mechanical behaviours, making them suitable for flexible applications in a wide range, including drug delivery, wearable communication, and sensors, most of the research studied in recent years focuses on fabricated devices on hard substrate. Due to the restriction of transferring procedures and extra complex fabrication process, little work has been done on the strain-modulation performance of low-dimensional based flexible p-n junction photodetectors.

Indium Selenide (In_2Se_3) owns high electrical mobility, excellent optical sensitivity and piezoelectric properties, which is highly promising as a piezophototronic material for the construction of flexible p-n heterojunction photodetector with p-type 2D TMDs. In_2Se_3 is known as a group III-VI multi-phase chalcogenide compound showing numerous benefits and has attracted extensive research interest in practical applications such as optoelectronic and photovoltaic devices. Among all existing phases, n-type α-In_2Se_3 has a moderate optical band gap of 1.4eV in bulk state and increase with decreasing thickness in 2D limit, demonstrating notable advances in photodetection prospective for a wide wavelength range. Also, on account of fast response time, efficient light absorption, outstanding photoresponse and high on/off ratio, α-In_2Se_3 is considered as an ideal material for heterostructure photodetectors.

This thesis presents the fabrication of flexible α-In_2Se_3/WSe_2 vdW heterostructure photodetector with a favourable structure design aiming to better optoelectronic behaviour by the piezo-phototronic effect. When the external mechanical deformation is applied to the flexible substrate, piezoelectric charges are generated at the In_2Se_3 side. The band slope near the p-n junction interface can be modulated by the charge induced piezo-potential. Also, the efficiency of photo-generated electron-hole pairs separation and transport can be further enhanced, which leads to an increase in photocurrent. The output current under 0.433% strain and 782 $\mu W/cm^2$ optical intensity can achieve 304 times larger than strain-free dark conditions. Also, the responsivity and detectivity can reach up to 4.61×10^5 A/W and 4.34×10^{14} Jones respectively. These results introduce a scheme in which flexible photodetectors' behaviour based on 2D materials can be improved by applying moderate external mechanical deformation. Furthermore, the novel 2D material based vdW heterostructure design can be inspired and extended to other synthetic optoelectronic applications.

List of Publications

Yuqian Zhao, Feng Guo, Ran Ding, Weng Fu Io, Sin-Yi Pang, Wenzhuo Wu, Jianhua Hao* "Piezo-phototronic effect in 2D α-In$_2$Se$_3$/WSe$_2$ vdW heterostructure for photodetector with enhanced photoresponse" ***Adv. Opt. Mater.*** 2021, 2100864 https://doi.org/10.1002/adom.202100864

Yuqian Zhao, Ran Ding, Feng Guo, Zehan Wu, Jianhua Hao* "Progress in piezo-phototronic effect on 2D nanomaterial based heterostructure photodetectors" Submitted as a chapter of the book **'*Functional Nanomaterials: Synthesis, Properties and Applications.'*** by Wiley-VCH, ISBN 978-3-527-34797-1

Feng Guo, Yongxin Lyu, Michal Bartlomiej Jedrzejczyk, **Yuqian Zhao**, Weng Fu Io, Gongxun Bai, Wenzhuo Wu, and Jianhua Hao* "Piezoelectric biaxial strain effects on the optical and photoluminescence spectra of 2D III–VI compound α-In$_2$Se$_3$ nanosheets" ***Appl. Phys. Lett.*** 2020, 116, 113101

Ran Ding, Yongxin Lyu, Zehan Wu, Feng Guo, Weng Fu Io, Sin-Yi Pang, **Yuqian Zhao**, Jianfeng Mao, Man-Chung Wong and Jianhua Hao* "Effective piezo-phototronic enhancement of flexible photodetectors based on two-dimensional hybrid perovskite ferroelectric single-crystalline thin-films" ***Adv. Mater.*** 2021,2101263

Acknowledgements

First and above all else, I would like to convey my deepest gratitude and admiration to my supervisor, Prof. Jianhua Hao, for his insightful advice, patient supervision, and inexhaustible encouragement during my postgraduate studies. His strong scientific knowledge and passionate attitudes toward science and research have greatly influenced my intention to accomplish my Mphil degree.

I also want to thank Prof. Siu Fung Yu and Prof. Yang Chai for their great help with my experimental study and course work. I would like to thank Dr. Terence Wong, Wong Hon Fai and Hardy Lui, and for their assistance with facility utilization in UMF and our department.

I appreciate my research colleagues, including Dr. Ran Ding, Dr. Beining Zheng, Dr. Man-Chung Wong, Ms. Wing Fu Io, Ms. Sin-Yi Pang, Ms. Yongxin Lyu, Mr. Feng Guo, Mr. Jianfeng Mao, Mr. Menglin Song and Mr. Zehan Wu for all the help they gave me during my investigations.

I gratefully thank the financial support from the Hong Kong Research Grant Council (RGC) of Hong Kong (RGC GRF No. PolyU 153023/18P).

Lastly, I would like to thank my parents, my two dogs (Jacky and Andy) and my dear friends, whom I will never forget for their support and endless love, is my eternal wealth.

Table of Contents

Table of Figures

Chapter 1 Introduction

1.1 Background of 2D materials

Two-dimensional (2D) materials are a group of ultra-thin, sheet-like crystals with atomic or molecular level thickness and lateral dimensions that are mainly characterized in micrometres. [1]Since Novoselov et al. and his group members isolated graphene effectively by mechanically exfoliating highly oriented pyrolytic graphite in 2004, prospective applications and fundamental interests have drawn widespread scientific attention.[2] 2D materials outperform their bulk counterparts in terms of tunable bandgap energy, high electron mobility, strong optical response, high thermal conductivity, remarkable environmental stability, and high mechanical flexible strength. [3]–[8] As 2D materials molecules possess strong intralayer covalent connections and weak interlayer van der Waals (vdW) forces between layers, they can be readily exfoliated and transferred to a flexible substrate without worrying about crystal lattice mismatch.[9] Furthermore, in 2D materials, interlayer van der Waals force exists instead of dangling bonds, resulting in the lack of point and line defects between layers, which suppresses recombination between non-radiative carriers and promotes photoelectric conservation.[10] In recent years, they have been widely investigated and utilized not just in electronics and optoelectronics incorporating flexible photoelectronics or optics, but also in electrochemical energy

storage devices such as solar cells owing to their ability in effective energy convertion. [11]–[18]

1.1.1 Transition metal dichalcogenides

Transition metal dichalcogenides (TMDs) are layered semiconductors of the form MX_2, where M is a transition metal atom (for example, Mo, Te, W etc.) and X is a chalcogen atom (for example, S, Se, Te etc.). [19]As illustrated in Figure 1.1, these materials exhibit layered structures of the pattern X–M–X, chalcogen atoms in two hexagonal planes bridged by a layer of metal atoms.[12], [20]
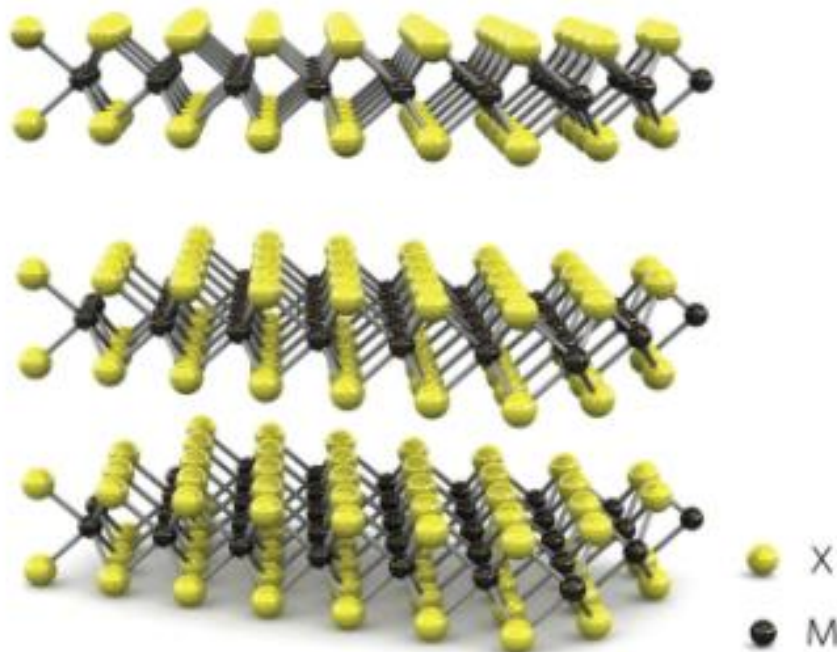
Figure 1.1 Schematic diagram of a 3D MX_2 structure. [21]

Figure 1.2 demonstrated that the adjacent layers are weakly held together by vdW interaction to form the bulk crystal in a range of structures that differ in stacking orders and metal atom coordination. The 2H corresponds to hexagonal symmetry, where the structure has two layers per repeat unit and trigonal prismatic coordination; 3R conform with the rhombohedral symmetry, where the structure has three layers per repeat unit and trigonal prismatic coordination; and 1T fits the tetragonal symmetry, where the structure has one layer per repeat unit and octahedral coordination.[22]–[24] TMDs have attracted numerous investigations in fundamental research in energy harvesting, flexible electronics and optoelectronics, spintronics, DNA sequencing, and personalized medicine owing to their unique combination of atomic-scale thickness, direct bandgap, strong spin-orbit coupling, and favourable electronic and mechanical characteristics.[25]–[27]
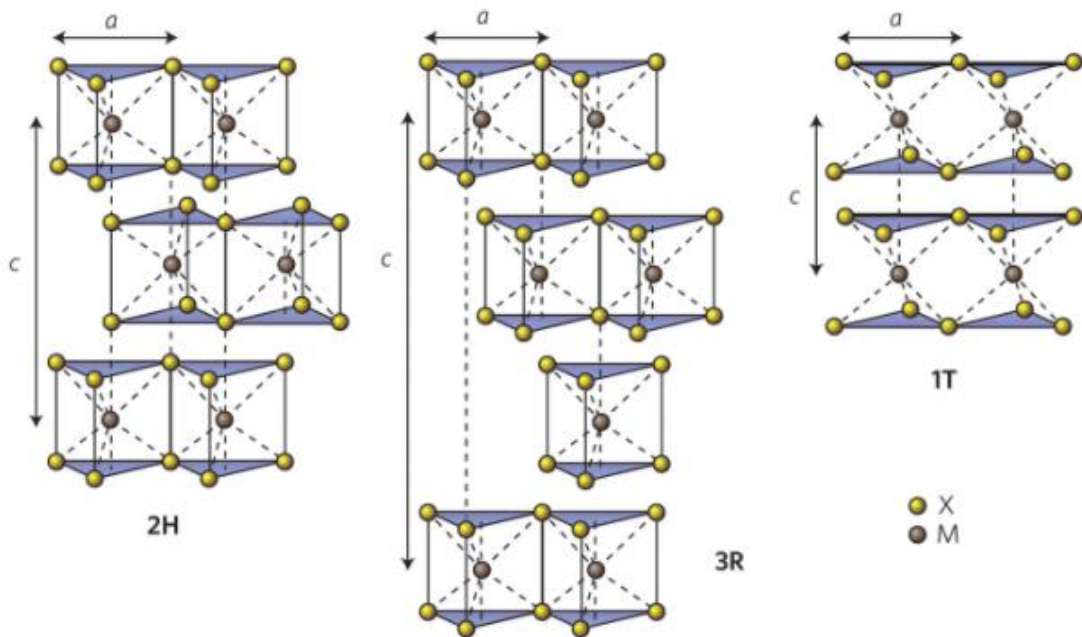
Figure 1.2 Crystal structures: 2H, 3R and 1T. The chalcogen atoms (X) are yellow and the metal atoms (M) are grey. [22]

1.1.2 Group III-VI compounds

Owing to the superior electrical and optoelectronic performance of typical 2D layered material group III-VI compound semiconductors M_2X_3 (e.g. M = Ga, In; X = S, Se, Te), they have generated considerable recent research interest.[28]–[33] M_2X_3s, like 2D TMDs, have substantial benefits such as atomic layer thickness, high surface area, and great compatibility. In comparison to TMDs, the M_2X_3 exhibits additional excellent properties like as high carrier mobility, great charge density, and so on. Indium selenide (In_2Se_3) is by far the most frequent M_2X_3 stoichiometry investigated multi-phase chalcogenide compound with numerous benefits that has sparked a lot of research in everyday applications including batteries, optoelectronics, and photovoltaics.[34]–[36] At different temperatures, five crystal structures (α, β, γ, δ, and κ) have been discovered, where γ-In_2Se_3 has a distorted wurtzite-like crystal structure; δ-In_2Se_3 has a monoclinic crystal structure and the rest of phases (α, β and κ) are layered structures. Among all phases, α-In_2Se_3 is considered as the thermodynamically stable one. The Se-In-Se-In-Se atomic layer forms a stable sheet via covalent bonds in each single-layer In_2Se_3, and the layers are linked by a weak vdW connection.[37] The α-In_2Se_3 demonstrates enhancements in the thickness dependent band gap when comparing to the other phases, as well as promising photodetection prospects for various wavelength.[36], [38] Because 2D α-In_2Se_3 films exhibits an anisotropic structure, they offer excellent stability, sensitivity, and optical, electrical, and transport characteristics. The presence of many defects in α-In_2Se_3 crystals [18] and their impact on anisotropic charge transport characteristics have lately been revealed. Kaminskii et al. and Zaslokin et al. have reported anisotropic conductivity in Mn, Cd, I, and Cu-doped In_2Se_3. [39]–[41] The electrical conductivity among layers is

significantly higher than the electrical conductivity across layers. Temperature dependent conductivity anisotropy has been utilized to calculate the energy barrier height between crystal layers. Peng et al. discovered a significant anisotropy of electrical conductivity up to 10^3–10^6 at ambient temperature in layer-structured α-In_2Se_3 nanowires. [42] Moreover, it exhibits ferroelectric properties and a particularly high liability at room temperature.[43], [44]
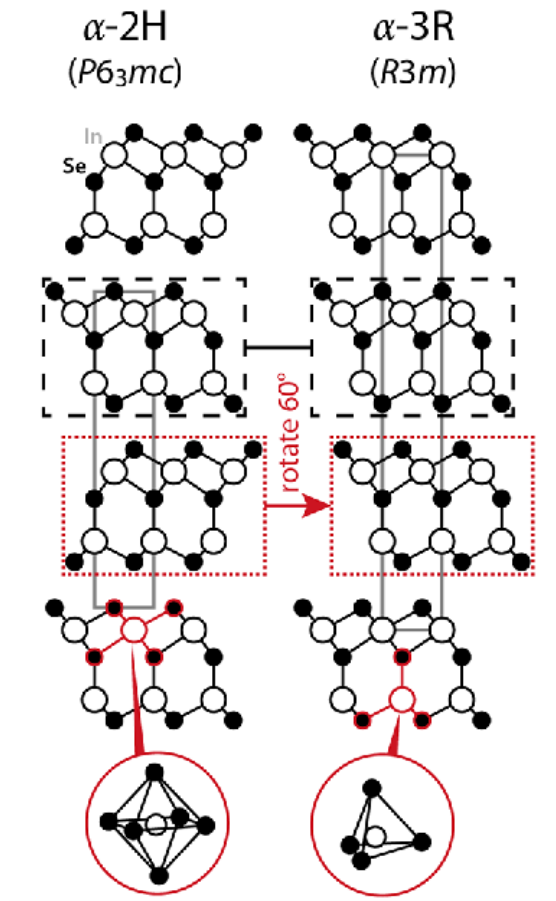
Figure 1.3 Schematic projection of α-2H and α-3R crystal structure of In_2Se_3[37]

1.1.3 Heterostructures based on 2D materials

Heterostructure is a semiconductor structure with non-uniform chemical composition, which effectively controls the states and motion of charge carriers (electrons and holes) in the active region. Once we combine several 2D materials in a vertical stack, a wide variety of possibilities arise. These heterostructures are held together by the vdW forces that maintain the layered materials together, allowing far more combinations than conventional synthesis process. Since the 2D material family expand rapidly, the complexity of heterostructures that can be constrated is increasing. Heterostructures of 2D materials provide extraordinary opportunities of combining them for technical applications. These stacks are different from 3D semiconductor heterostructures, where each layer functions as bulk material and interface at the same time, diminishing displacement of charges within every single layer. Even so, charge transfers between layers could be quite large, resulting in large electric fields and motivating band-structure engineering opportunities. Many interesting physical phenomena have already been discovered as a result of such heterostructures. Several groups were able to examine the Hofstadter butterfly effect and topological currents in a graphene interacting with hBN system with using spectrum reconstruction. The ability to place crystals in close (but regulated) contact to one another enables the investigation of tunneling and drag effects. The application of semiconducting 2D materials results in the development of optically active heterostructures. Because such heterostructures have a wide range of functions, they may be used for a variety of purposes. By integrating optically active semiconducting layers together, photovoltaic and light-emitting devices have been developed.

Vertical vdW heterostructures are most easily fabricated by a multi-step mechanical transfer of 2D layers onto a substrate, such as manipulating individual nanosheets one after another (shown in Figure 1.4). In theory, these transfer process can also be applied to fabricate bottom-up high-quality multiple-layer vdW heterostructures. The carrier foil transfer and stamping, classified as a developed transfer method, are different from the following basic schemes. Whether the 2D layer must be transferred from the growth substrate or can be mechanically exfoliated straight away on top of the transfer polymer determines this approach.
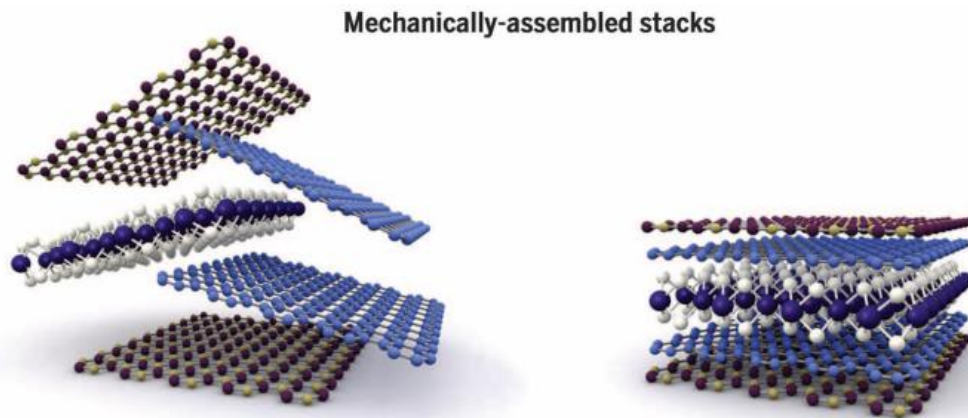
Figure 1.4 Schematic production of vdW heterostructures through mechanical stacking[9]

Other than the major of direct stacking of individual 2D flakes among various materials, approaches for transferring large-area crystals produced by chemical vapor deposition (CVD), direct synthesis of heterojunction by CVD or physical epitaxy, and one-step growth in solution are also explored, as presented in Figure 1.5. CVD and other direct growth methods are potential strategies for scalable fabrication of vdW heterostructures.

These procedures can be classified into three groups, including successive CVD development of 2D crystals onto the mechanically transferred or grown 2D flakes, vapor-solid processes for direct construction of TMDs heterojunctions, and vdW epitaxy. Many vertical heterostructures have previously been constructed with these methods.[45]–[49]
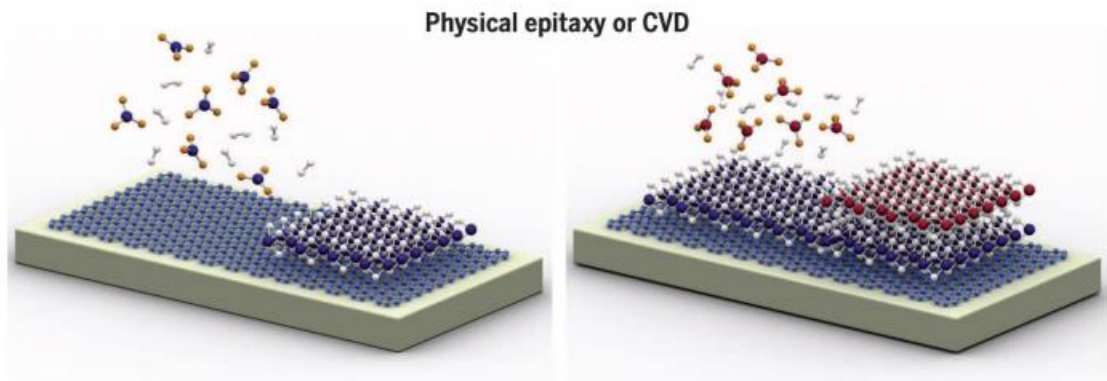
Figure1.5 Schematic production of vdW heterostructures CVD or physical epitaxy growth[9]

1.2 Photodetectors based on 2D materials and their heterostructures

A photodetector is an electronic device that can identify optical signals and is potentially applicable in imaging technologies, safety monitoring sensors, communication devices, and primary research purposes.[50], [51] W. Smith identified photoconductivity in selenium in 1873, and this was the foundation of photo-detectors.[52] In 2009, an ultrafast graphene photo-detector based on 2D materials was first constructed, which functioned

without external bias voltage and exhibited robust photo-response for optical modification up to 40GHz.[53], [54] Graphene, being the archetypal 2D material, offers great carrier mobility, a wide absorption spectrum, and a short reaction time, all of which are required for high-performance photodetectors.[55], [56] Nevertheless, graphene's low absorbance is a significant constraint, and the greatest photoresponsivity based on an exfoliated graphene photo-detector so far is 6.1 mA/W[57]. The efficient construction of few-layer 2D transition metal dichalcogenide semiconductors (TMDCs) with substantially higher optical absorption has recently extended this limitation by many orders of magnitude, resulting in significantly enhanced photodetector performance.[58], [59] For instance, a photodetector based on exfoliated monolayer MoS_2 has a photoresponsivity of 880 A/W at 561 nm[60].
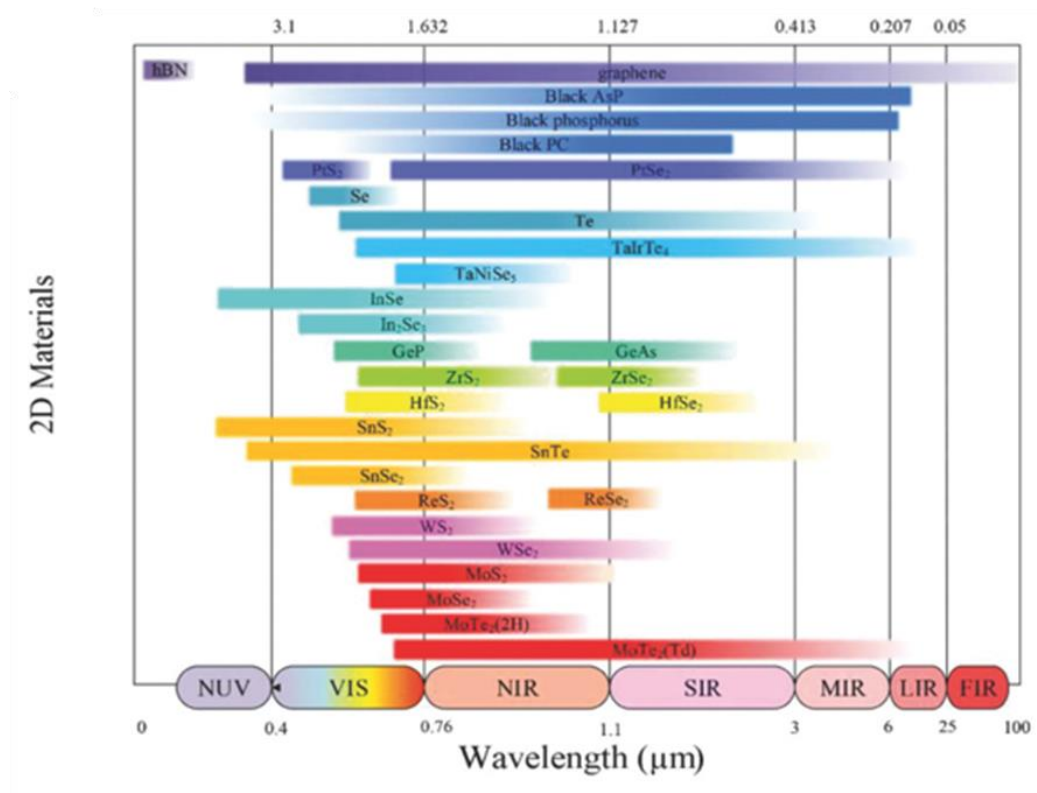
Figure 1.6 Bandgap and detection regions of variable 2D materials [61]

2D material heterostructures give a better development of flexible electronic devices for future generations and offer possibilities for high-performance vdW devices with configurable material features such as rapid photoresponse and strong light interaction.[62], [63] When different materials with different work functions are combined, photoexcited electrons and holes accumulate in different layers, promoting the indirect excitons. These excitons usually have long lifetimes, and their binding energy can be optimized by varying the distance between the semiconductor layers.[64] Moreover, heterojunction constructed with variable materials can combine various material properties to enhance device performance.[65], [66] Table.1 below listed the parameters widely used to evaluate the performance of photodetectors.

Table.1 Parameters used to evaluate the performance of photodetectors

Parameters	**Expression**	**Unit**	**Definition**
Photocurrent	$I_{ph} = I_{light} - I_{dark}$	A	I_{light} is the output current under light illumination, and I_{dark} is the output current tested under dark condition
Photoresponsivity	$R = \dfrac{I_{Ph}}{P}$	A/W	I_{Ph} is the photocurrent, and P is the optical illumination intensity
Response time	τ_r/τ_f	s	The τ is defined as the time required for the current rise or fall from 10% to 90% or 90% to 10%
Noise equivalent power	$NEP = \dfrac{in}{R}$	W Hz$^{1/2}$	*in* is defined as the noise current of device

Specific detectivity	$D^* = \dfrac{\sqrt{A}}{in} R_i$	cm Hz$^{1/2}$ W^{-1} (Jones)	A is the effective area (unit of cm^{-2}) of device
External quantum efficiency (EQE)	$EQE = R_i \dfrac{hv}{e}$	%	hv is the energy of one single photon, e is unit electron charge

1.3 Concept of piezoelectric and piezophototronic effect

1.3.1 Fundamental Physics of piezoelectric and piezophototronic effect

The piezoelectric effect is a phenomenon that an electric field is generated in response to mechanical stress in certain materials. The direct piezoelectric effect is electricity generated with applied stress, whereas the converse piezoelectric effect refers to the generation of stress under an electric field. The polarization of ions is induced when a strain applied to a non-central symmetric structure crystal. The anions and cations split from the relative centres of the crystal structure, resulting in the formation of a dipole momentum and the dipole contribution leads to piezo potential generation. [67]–[70]
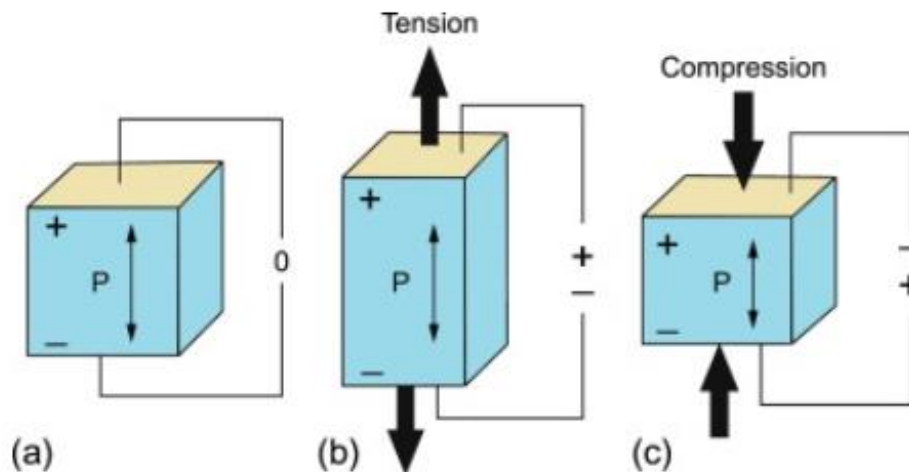
Figure 1.7 Schematic diagram of piezo-polarization generation [71]

Wang et al. coined the term piezophototronic after discovering piezoelectric generation in ZnO nanowires. [72] Piezotronics are electronics that are using the potential barrier to modulate and control the charge transport behaviour by the piezoelectric effect as the gate voltage at the interface. The barrier height can be modified by applying tensile or compressive strain. Due to the piezoelectric effect, electron transport at the barrier becomes tunable. When the barrier is lowered, more electrons can move through, and vice versa.[73], [74] Continuously increasing the height of the barrier results in a cut-off current, which is comparable to the property of diodes. The piezotronics effect refers to the manipulation of piezoelectric potential to regulate electronic transport across interfaces between metal and semiconductors or junction between p-type and n-type semiconductors.

The combination of piezoelectric polarization and photonic excitation in non-central symmetry crystals is known as the piezophototronic effect. Wang first revealed in 2010 that, while the piezoelectric action raises the Schottky barrier, photon excitation lowers the height of the Schottky barrier as carrier density increases.[75]

The performances of optoelectronic devices such as photodetectors, light-emitting diodes, and solar cells are controlled by piezo-potential as a gate voltage to alter charge production, transportation, and recombination, allowing the optoelectronic process to be tuned.[76], [77]
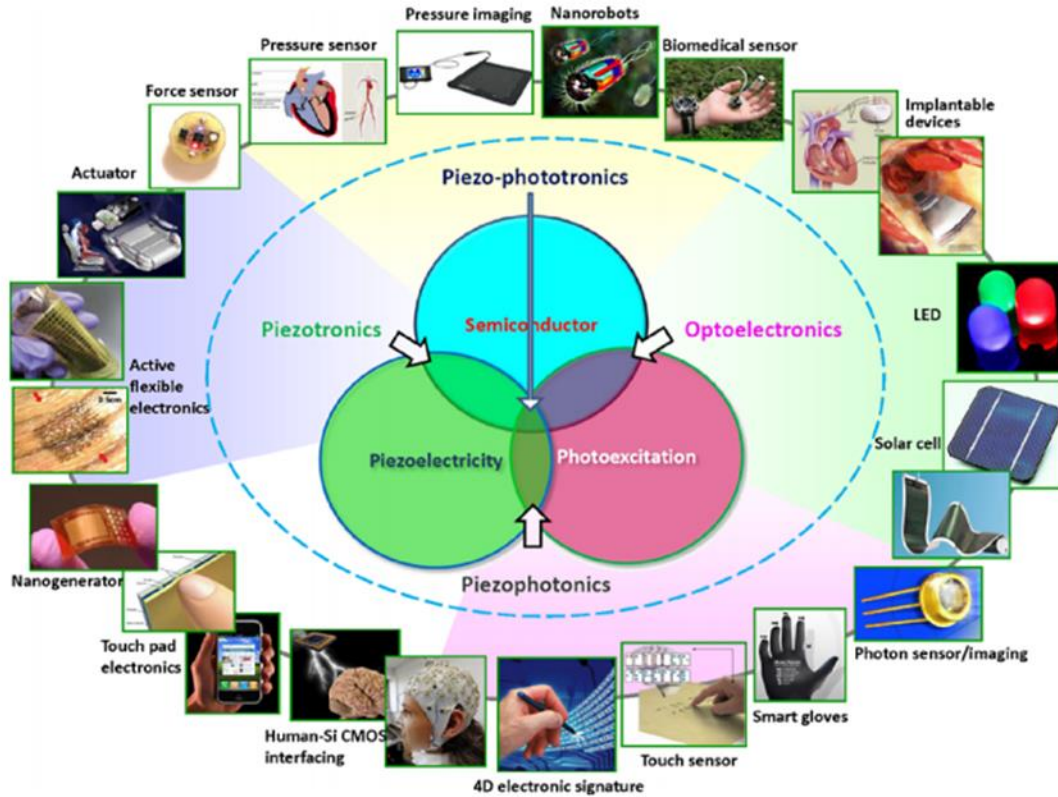
Figure 1.8 Schematic diagram of piezo-phototronic effect based on three way coupling among semiconductor, piezoelectricity and photoexcitation and related applications in these research fields.[78]

1.3.2 Piezoelectricity and Piezophototronic effect induced in α-In$_2$Se$_3$

The atomic arrangement "ABC" in a single layer projects a basic hexagonal structure among in-plane direction, as seen in the top panel of Figure 1.9, each kind of atom organized in a triangular lattice at the six vertexes. Since the two Se atoms and one In atom have non-equivalent locations, such a hexagonal configuration clearly lacks of centrosymmetry.
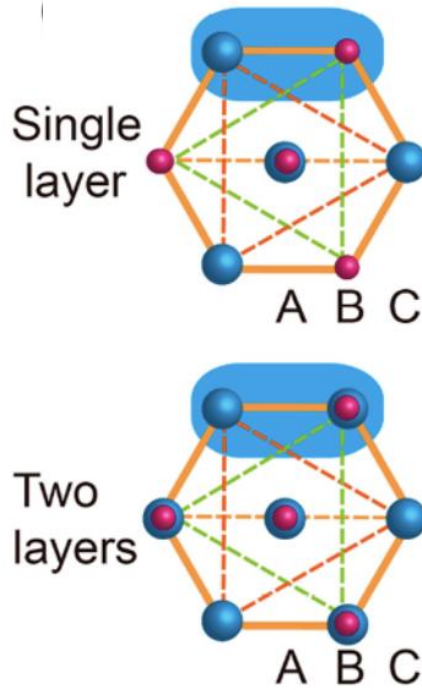
Figure 1.9 Atomic structure of α-In$_2$Se$_3$ at top panel [79]

As spotted by the pink arrow in Figure 1.10, a charged electric dipole can form from a planar strain, resulting in an in-plane (d_{11}) piezoelectric field.[79]
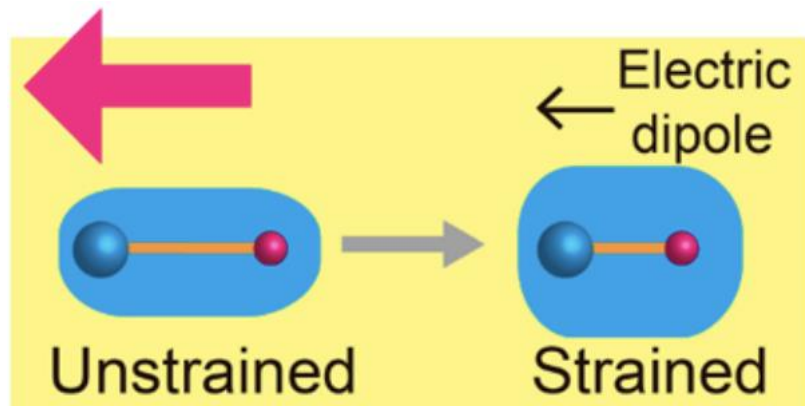
Figure 1.10 Schematic diagram of α-In$_2$Se$_3$ with application of lateral strain[79]

It has been reported that the lateral piezoresponse force microscopy (PFM) results show distinct amplitudes as the sample thickness changes. The in-plane piezoresponses show an increasing trend until the thickness reaches 90 nm, after that, the piezoresponses exhibit a saturated level. The author suggests that this strongly linked shift in both in-plane piezoelectric behaviours should be attributed to a diminishing substrate clamping effect with increasing tested thicknes. In conclusion, regardless of thickness, this hexagonal α-In$_2$Se$_3$ retains in-plane piezoelectricity.[79]
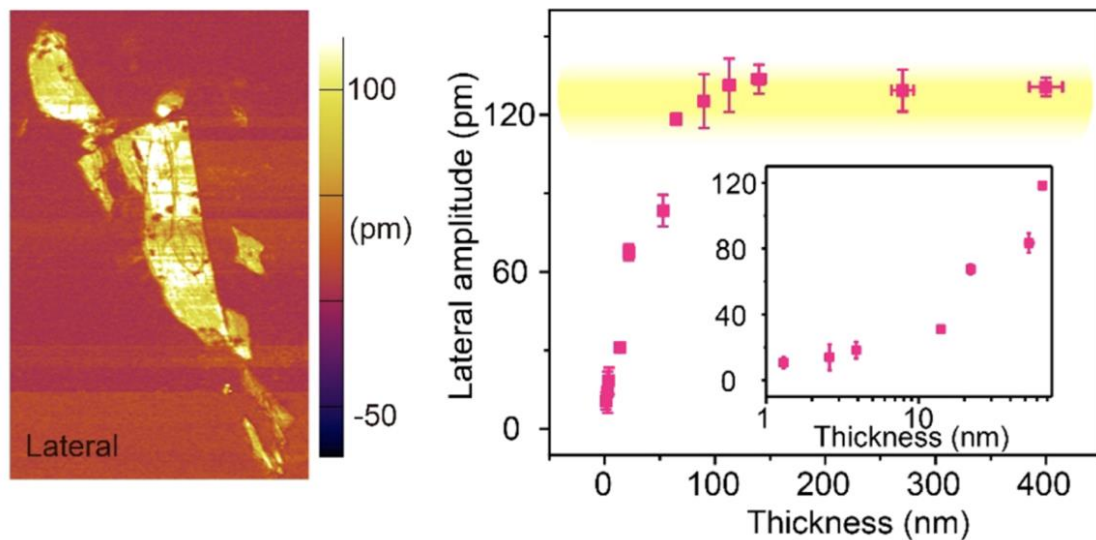
Figure 1.11 Left: Lateral PFM image of α-In$_2$Se$_3$ Right: Lateral amplitude as a function of α-In$_2$Se$_3$ nanoflake thickness.[79]

1.4 Piezo-phototronic effect impact on Schottky contact photodetectors

When the metal comes into contact with the semiconductor, Fermi energy of metal and semiconductors adjust to the same level. The metal-semiconductor system reaches equilibrium after charges redistribute notably in the junction area.[80], [81] The height of the Schottky barrier at the metal-semiconductor interface may be utilized to calculate charge carrier mobility at the interface.[82] Schottky barrier height (SBH) is used to assess the mismatch of energy bands. When a semiconductor is compressed along the c-axis, the strain causes a negative polarization charge to develop and electrons to be repelled from the interface. SBH increases with increasing depletion zone width (as illustrated in Figure 1.12). Since the separation and collection of electrons and holes has been enhanced, the photocurrent has increased.
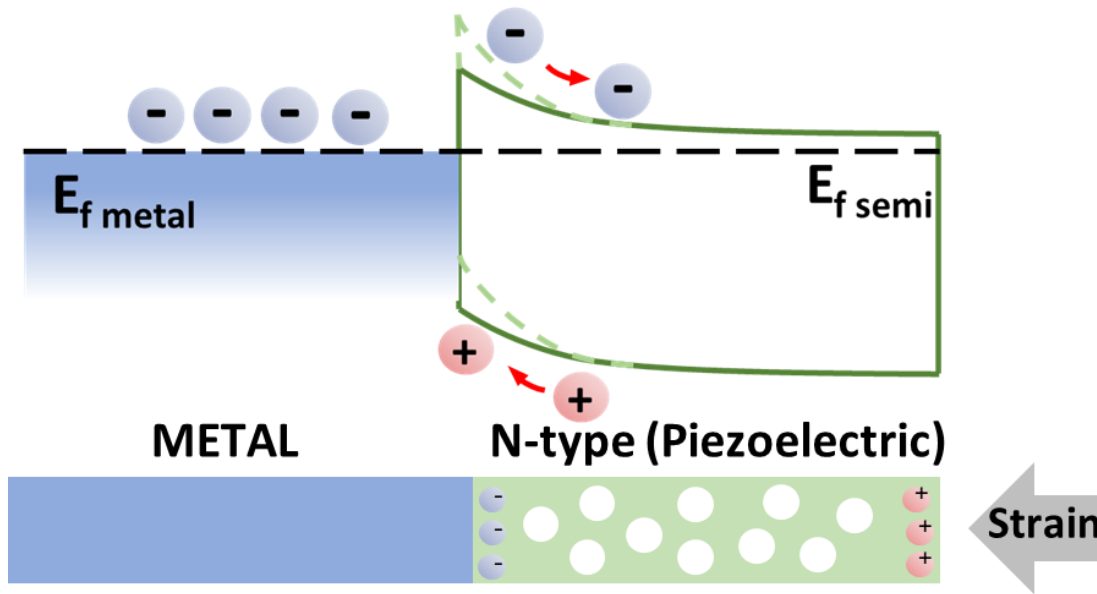
Figure 1.12 Schematic diagram of piezo-phototronic effect in Schottky junction under

compressive strain conditions

Tensile strain, on the other hand, induces a positive polarization charge. As shown in the

Figure 1.13, electrons are drawn to the interface, reducing the width of the depletion

zone and lowering SBH. When a photo-sensitive metal-semiconductor Schottky barriers

is subjected to a light source, incoming photons produce electron-hole pairs in the

semiconductor. Electric field modulation can be used to modify the photocurrent

generated by the separation and collection of electrons and holes in the Schottky

junction. [80]
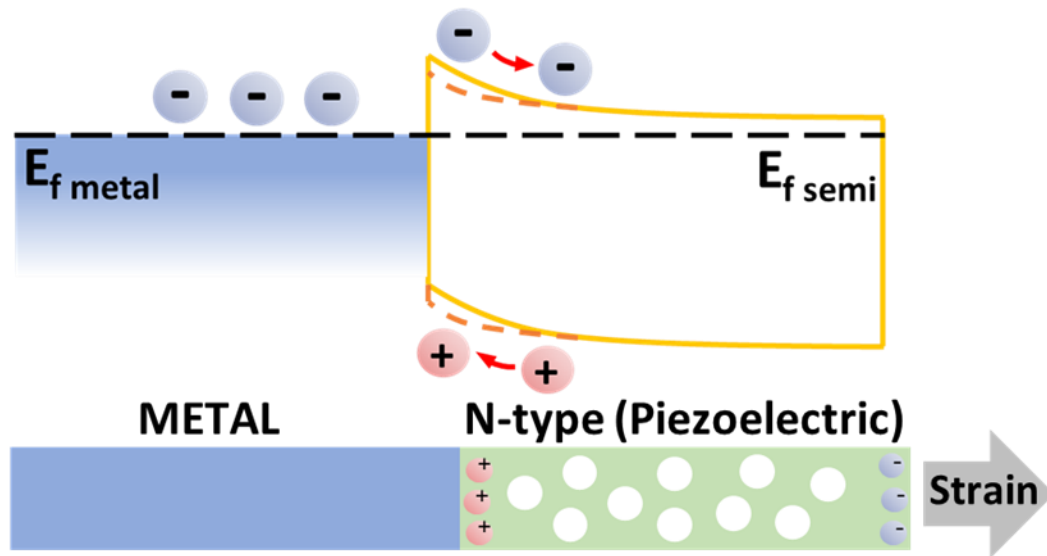
Figure 1.13 Schematic diagram of piezo-phototronic effect in Schottky junction under

tensile strain conditions

We have discussed that the construction of Schottky junctions and the SBH concept contribute to the photodetection mechanism. Through regulating the SBM, sensitive photodetectors with a high gain and fast response can be achieved. A typical piezotronics device has two basic structural configurations. Two back-to-back Schottky contacts between metal and piezo-semiconductor, as well as a semiconductor channel, make up one structure. [65] As some of the piezoelectric 2D semiconducting materials show exclusive optoelectronic properties due to their bandgap size, when strain is applied to the photodetector constructed with these materials, a polarization charge is then generated in the vicinity of the interface. Also, the barrier height is modulated. The performance of the photodetectors can be coordinated when charge carriers separate and transfer at the Schottky barrier interface by the piezo-phototronic effect, resulting in generation of piezo-

potential. Theoretically, applying strain decrease can modulate the valance band maximum and the conduction band minimum, which leads to the modification of the SBH and the photocurrent. Therefore, the photodetection performance of the photodetectors can be moderated by the piezo-phototronic effect.[83]

1.5 Piezo-phototronic impact on P-N junction based photodetector

A material with an n-type property has been doped using electron donors. In n-type materials, the number of electrons increases while the number of holes decreases. The effective Fermi level is moved midway between the donor and conduction bands. The p-type doped area has a lower electron concentration and a higher work function, resulting in a reduction in the Fermi level and a shift toward the valance band. When a p-type semiconductor is in contact with an n-type semiconductor, a p-n junction forms at the interface. Suppose the p-type side has a relatively positive external voltage bias than the n-type, current would travel more efficiently in the p to n direction, also known as forwarding bias and forward current. When the p-type side is more negative than the n-type, no current will flow; that is called reverse bias and reverse current. This asymmetric current flow characteristic of p-n junctions makes them very suitable for constructing modern electronic devices. When p-type is positive with respect to n-type (forward bias), electrostatic potential increases on the p-type side rather than the n-type side hence lowering the electrostatic potential barrier. In contrast, the electrostatic potential would become larger if reverse bias is applied, as the p-type side is depressed relative to the n-

type side. The drift current of both electrons and holes are from n side to p side. Though electrons and holes have opposite particle flow directions, their diffusion current is from p side to n side. The sum of drift and diffusion current is known as total current flow through the junction. At equilibrium, the net current equals 0. The net currents of electrons and holes are both zero, which means the diffusion and drift components cancel out. The large barrier would occur at the junction under reverse bias so that both diffusion components are inappreciable. The relatively small generation current constitutes the net current because of the carrier collection in the transition region or diffusion of minority carriers to the junction from n-type to the p-type semiconductor. Under forward bias, the probability of carrier diffusion across the junction increases, which leads to an increase in current.

The alternative construction consists of two Ohmic contacts and a p-type/n-type semiconductor junction.[1] Strain-induced piezo-charges modify energy bands at the p-n junction the same way as SBH is adjusted in a Schottky contact. Under strain-free conditions, the centres of positive and negative charges are identical. Near the p-n junction, the space charges generated by ionized donors and acceptors form a built-in electric potential that improves photo-generated carrier separation under illumination.[84], [85] When light reaches a p-n junction, electron and hole pairs are formed. With an electric field present, photogenerated carriers pass through the depletion layer, generating a photocurrent. [86], [87] When a compressive strain is applied to a p-n junction with only n-type material having piezoelectric properties along the c-axis, negative piezo polarization charges are generated at the interface on the n-type side of the depletion zone. The depletion area increases gradually and moves to the n-type side. The resistance to the

contact reduces as a result of the charge injection, resulting in a rise in current. Because of the piezo-charge, the edges of bands bend upwards, suppressing electron and hole recombination. This enhances photogenerated carrier separation (as shown in Figure 1.14).
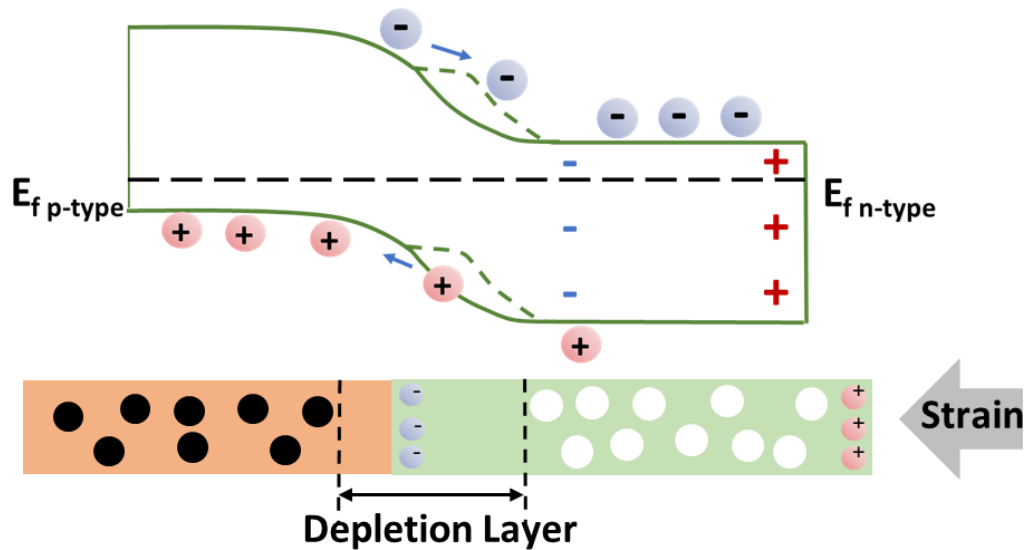
Figure 1.14 Schematic diagram of piezo-phototronic effect in p-n junction under compressive strain condition

On the contrary, positive polarization induces and draws electrons to the contact when a tensile strain is applied. The depletion zone grows and moves to the p-type semiconductor side. Photon absorption is thus enhanced, resulting in a profusion of carriers on the p-side. A dip is caused by positive polarization charges near the band edge of the n-type side, where photogenerated carriers prevent electrons and holes from separating, resulting in a reduction in photocurrent (presented in Figure 1.15).[78]
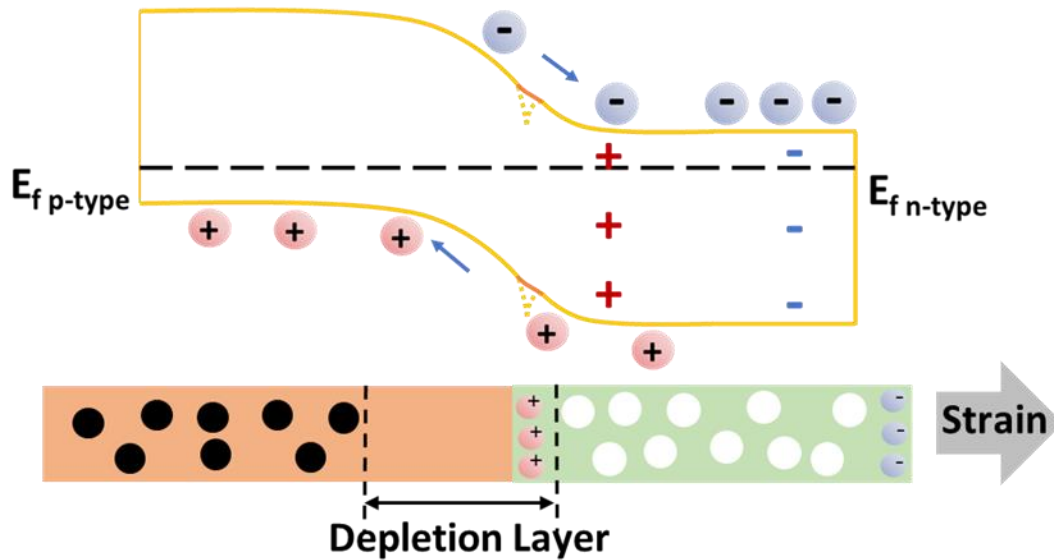
Figure 1.15 Schematic diagram of piezo-phototronic effect in p-n junction under tensile

strain conditions

In conclusion, when light illuminates on the p-n junction, photon absorption generates electron-hole pairs. The carriers travel through the depletion layer by the built-in electric field, leading to the formation of photocurrent. With the application of strain, polarization charges introduced result in the deformation of the depletion zone. This affects the effective resistance for carrier transport at the interface, thus modulating the photocurrent.

1.6 Objective of the research

Since graphene was exfoliated successfully from highly oriented pyrolytic graphite mechanically in 2004, two dimensional (2D) materials have attracted widespread interest due to their distinctive morphology and optoelectronic properties that are unattainable in

bulk states. Beyond 2D semimetal, transition metal dichalcogenides (TMDs), known as a class of representative 2D semiconductors, have various work functions and adjustable energy band gaps, making them appropriate for the construction of van der Waal (vdW) heterostructures with variable characteristics. In recent years, dangling bond free 2D-layered semiconducting materials have been frequently used as fundamental material to build up heterostructure in multiple applications due to the absence of traditional consideration of lattice mismatch during contact. Besides, reducing the interface defects reduces the photoelectric conversion in 2D crystals as the recombination of carriers has been suppressed. Moreover, numerous experiments have established that several monolayer or few-layer 2D semiconductors involving TMDs and III-VI compounds possess significant piezoelectric and optical properties, indicating that the performance of optoelectronics can be modulated directly by accumulating external strain.

This study investigated that, with the application of external mechanical strain, the performance of photodetector can be strain-modulated based on the remarkable piezoelectric property of few-layer α-Indium Selenide (α-In$_2$Se$_3$). The piezo-phototronic effect is a unique three-way coupling between photoexcitation, piezoelectric and semiconducting properties, attracting significant attention due to the possible modulation to the generation, transportation, separation, and recombination of the photo-excited charge carriers near the metal-semiconductor Schottky contact and P-N junction by the strain-induced piezo-potential. Since Wang first proposed the piezo-phototronic effect in 2010, flexible optoelectronic devices, including photodetectors, solar cells and light-emitting diodes, have mainly been improved with the application of external strain.

Previous studies have demonstrated the strain-modulated photoresponse in mixed-dimensional heterostructure photodetectors, such as the combination of one-dimensional (1D) n-type piezoelectric wurtzite-structured nanowires (e.g. CdS, ZnO) and two-dimensional (2D) p-type transition metal dichalcogenides (TMDs) (e.g. WSe_2). After indicating the piezo-phototronic effect in monolayer MoS_2 by Wu in 2016, a few reports were further established on piezoelectric MoS_2-based P-N heterojunction photodetectors. However, the photoresponse enhancement of MoS_2-WSe_2 based photodetector was relatively inconspicuous under compressive strain conditions, while the study of CuO-MoS_2 photodetector only discussed the performance of the device under tensile strain conditions. Moreover, the problem of only having a direct bandgap at monolayer condition fundamentally restricting the application of TMDs in the photoelectronic field due to poor light absorption and small current carrying capacity. In stark contrast, Indium Selenide (In_2Se_3) owns high electrical mobility, excellent optical sensitivity and piezoelectric properties, which is highly promising as a piezophototronic material for the construction of flexible P-N heterojunction photodetector with p-type 2D TMDs. Due to their photoelectric characteristics, III-VI layered semiconductors have been the subject of numerous theoretical and practical research in recent years, and the related photovoltaic, switching, and memory devices have been manufactured [27-28].

In this thesis, we would like to present a flexible α-In_2Se_3/WSe_2 van der Waals (vdW) P-N heterojunction photodetector with a favourable structure design aiming for better optoelectronic behaviours the piezo-phototronic effect. When the external mechanical deformation applied to a flexible substrate, piezoelectric charges generated at the In_2Se_3 side. The band slope near the p-n junction interface was modulated by the charge-induced

piezo-potential, further enhancing the efficiency of photo-generated electron-hole pairs separation and transportation and thus leading to an increase in photocurrent. Furthermore, novel 2D material-based vdW heterostructure designs can be inspired and extended to other synthetic optoelectronic applications.

1.7 Organization of thesis

The thesis chapters are organized as follow:

Chapter 1 Introduction: This chapter begins by providing an overview of common 2D vdW layered materials, including their unique characteristics and variable utilizations. The structure of vdW materials, as well as techniques for constructing 2D vdW heterostructures and construction of heterojunction photodetectors, are briefly explained after that. Then, the fundamental theory of piezoelectric and piezophototronic effect have been explained. Lastly, the modulation mechanism of piezo-phototronic effect on Schottky barrier and p-n junction have been discussed.

Chapter 2 Experimental methods: The experimental approaches used in this thesis are described in this chapter. The fabrication processes used to prepare the ultrathin 2D materials are first discussed. Following that, the approach used for characterizing 2D flakes and assembling vdW heterostructures photodetectors based on them are presented. Finally, the set up for electronic and photoelectronic characterization of devices under different strain conditions are described.

Chapter 3 Fabrication and Characterization of α-In$_2$Se$_3$ and WSe$_2$: This chapter explores the fabrication of α-In$_2$Se$_3$ and WSe$_2$ nanoflakes, and demonstrated the construction of their heterostructures. After that, they are characterized by the approaches discussed in Chapter 2.

Chapter 4 Flexible photodetectors based on α-In$_2$Se$_3$/WSe$_2$ vdW heterostructure: The performance of flexible photodetectors based on α-In$_2$Se$_3$ and WSe$_2$ heterostructure has been studied under different strain and light illumination intensity conditions. These results introduce the behaviour of these flexible photodetectors can be improved by applying moderate external mechanical deformation with the piezo-phototronic effect.

Chapter 5 Conclusion and future perspectives: The results of this work are summarized in this chapter. Furthermore, the future prospects of 2D piezoelectric and their heterostructures, as well as associated applications, are discussed.

Chapter 2 Experimental Methods

The primary experimental methods used in this thesis will be introduced in this chapter. The nanoflakes were prepared through mechanical exfoliation. The Raman and PL spectra of the samples were measured by a Raman system. The chemical composition was analysed with an X-ray photoelectron spectroscopy (XPS). The surface topography and thickness of the samples were characterized by the atomic force microscopy (AFM). The *I-V* curves of the devices were measured by a semiconductor analyzer. The strain was applied with a home-made bending apparatus and the red light-emitting diode (LED) was used as a light source.

2.1 Fabrication method of 2D materials

Mechanical exfoliation and chemical vapour deposition (CVD) are typical examples of physical and chemical few-layers material fabrication method, respectively. Particularly, physical methods show advantages in ease of preparation, good chemical stability and low cost. The principle and fabrication procedures of the mechanical exfoliation utilized will be described in following section.

2.1.1 Mechanical exfoliation

Mechanical exfoliation is one of the most widely used methods for 2D nanoflake fabrication, which is applying a force to break the vdW interaction between the bulk

crystal layers with scotch tape. In the meantime, the in-plane covalent bonds of each layer remain unbroken, which results in peeling off monolayer or few-layer 2D flakes. We press the adhesive side of a scotch tape onto the 2D bulk crystal, and the tape with crystals stuck on is pasted up and torn apart several times with another adhesive tape surface to obtain appropriately thin and uniform nanoflakes. Then the tape with 2D layered materials is adhered to the target substrates. As presented in Figure 2.1, some of the monolayer and few-layer thin flakes left on the substrate after peeling off the tape. When a suitable substrate is employed, the exfoliated samples can be observed with the optical microscope.[88] Despite mechanical exfoliation is a random technique, whose yield highly depends on various condition, the samples with high quality and clean surface can be obtained on arbitrary substrate with the method at room temperature. All multilayer α-In_2Se_3 and WSe_2 flakes used in this thesis were mechanically exfoliated from bulk crystals that were purchased from HQ graphene.
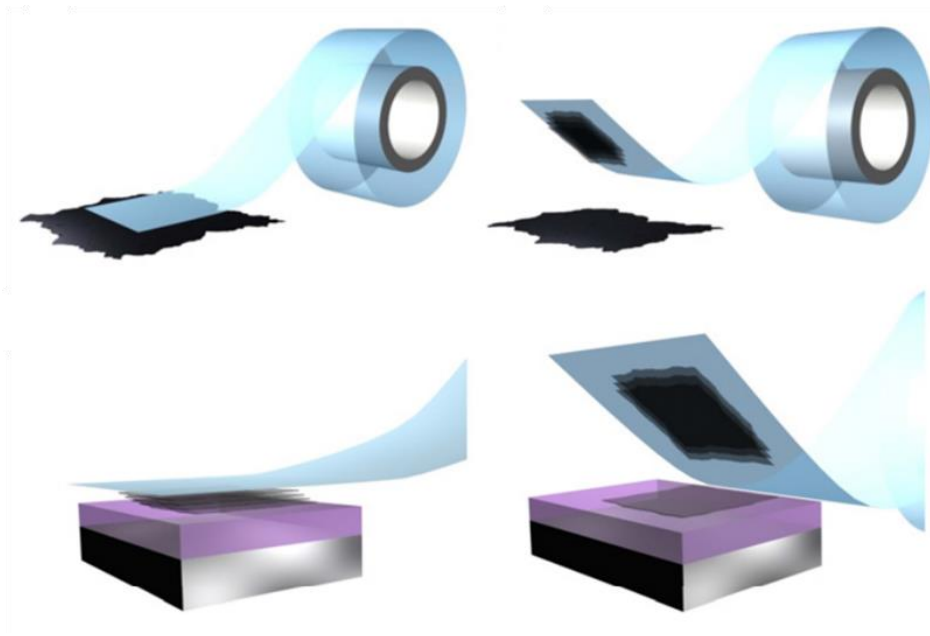
Figure 2.1 Schematic diagram of typical mechanical exfoliation process.[88]

2.2 Characterizations for 2D nanoflakes

2.2.1 Optical microscope

The optical microscope is a simple and effective way to deduce information regarding the location, shape and thickness of the sample materials. The operation principle of an optical microscope is the interference of reflected light at a distinct media interface. The optical contrast between bare substrates and 2D materials is produced when the sample introduced considerable optical paths and opacity perturbations. Among all kinds of substrates, silicon coated with 285 nm silicon dioxide (SiO_2/Si) is most commonly used for 2D material observation. Part of the incident light is transmitted, whereas the other part is

reflected at each interface. The intensity of the collective reflected light about interference varies with position and is affected by sample thickness, absorption coefficient, and refractive index variation.

2.2.2 X-ray diffraction

X-ray is classified as a non-destructive technique to investigate the crystallographic structure. XRD is a technology that utilizes irradiating a material with incident X-rays and then determining the intensities and angles of the scattered beams that leave the material. The identification of materials based on their diffraction pattern is one of the most common applications of XRD analysis. XRD provides information on how the practical structure differs from the ideal one due to internal tensions and defects, in addition to phase identification. X-rays are waves of electromagnetic radiation, whereas crystals are ordered arrays of atoms. The interaction of incident X-rays with the electrons of crystal atoms scatters incident X-rays. Elastic scattering is the name for this process, and the electron is the scatterer. A regular array of spherical waves is created by the scatterers of a regular array. These waves cancel each other out in major directions due to destructive interference, but they contribute constructively in a few particular directions, as specified by Bragg's law:

$$2d \sin \theta = n\lambda$$

where d is the distance between parallel diffracting planes, θ is the incident angle, n is an integer, and λ is the X-ray beam wavelength. The precise directions show as reflections on the diffraction pattern. As a result of electromagnetic waves impinging on a regular

array of scatterers, X-ray diffraction patterns form. Because the wavelength of X-rays is often the same order of magnitude as the spacing between the crystal lattices (1-100 angstroms), they are used to generate the diffraction pattern. XRD plays a major role in determining atomic arrangement and crystal characteristics, including lattice parameters, strain, grain size, phase composition and so on.
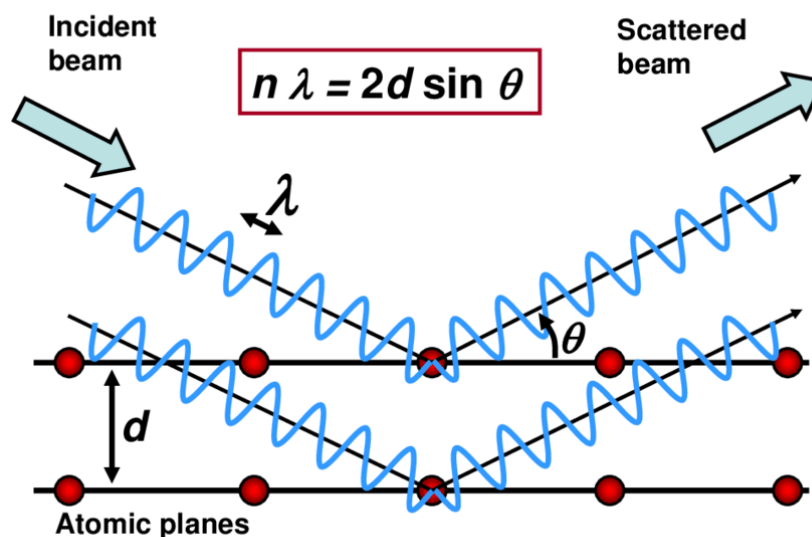
Figure 2.2 Working principle of X-ray diffraction [89]

2.2.3 Raman spectroscopy

The Raman Spectroscopy, a non-destructive chemical analysis technique, gives precise information on chemical structures, phases, polymorphs, crystallinity, and molecular interactions based on the interaction between incident light and the chemical bonds of the material. Raman is a light scattering method in which incoming light from a high-intensity laser light source is scattered by a molecule. Rayleigh scatter occurs when most

of the scattered light has the same wavelength as the laser source and provides no valuable data. Nonetheless, Raman scatter occurs when a tiny quantity of light (usually around 0.0000001%) is scattered at different wavelengths depending on the chemical structure of the sample. The intensity and wavelength location of Raman scattered light can be observed in a Raman spectrum, which is a series of peaks. When the incident light is scattered by a molecule, the molecular electron cloud polarization is induced by the oscillating electromagnetic field of a photon. This places the molecule in a higher energy state as photon energy transferred to the molecule. The generation of a very short-lived complex between the photon and the molecule, known as the virtual state of the molecule. The photon is re-emitted as scattered light quite rapidly since the virtual state is not stable. The Stokes Raman scattering (named after G.G. Stokes) is known as molecule receives energy from the photon and stimulated to a higher vibrational state during scattering, the scattered photon loses energy results in increasing wavelength. On the contrary, anti-Stokes Raman scattering occurs when a molecule loses energy by relaxing to a lower vibrational state. The scattered photon gains the equivalent energy thus the wavelength decreases. Stokes and Anti-Stokes processes happens at similar rates quantum mechanically. Nevertheless, in a group of molecules, most of them are statistically more likely to be in the ground vibrational level (Boltzmann distribution), and Stoke scattering shows a higher probability statistically. Consequencely, the anti-Stokes scattering is less intense than the Stokes scattering, thus in Raman spectroscopy, the Stokes Raman scatter is more often detected.
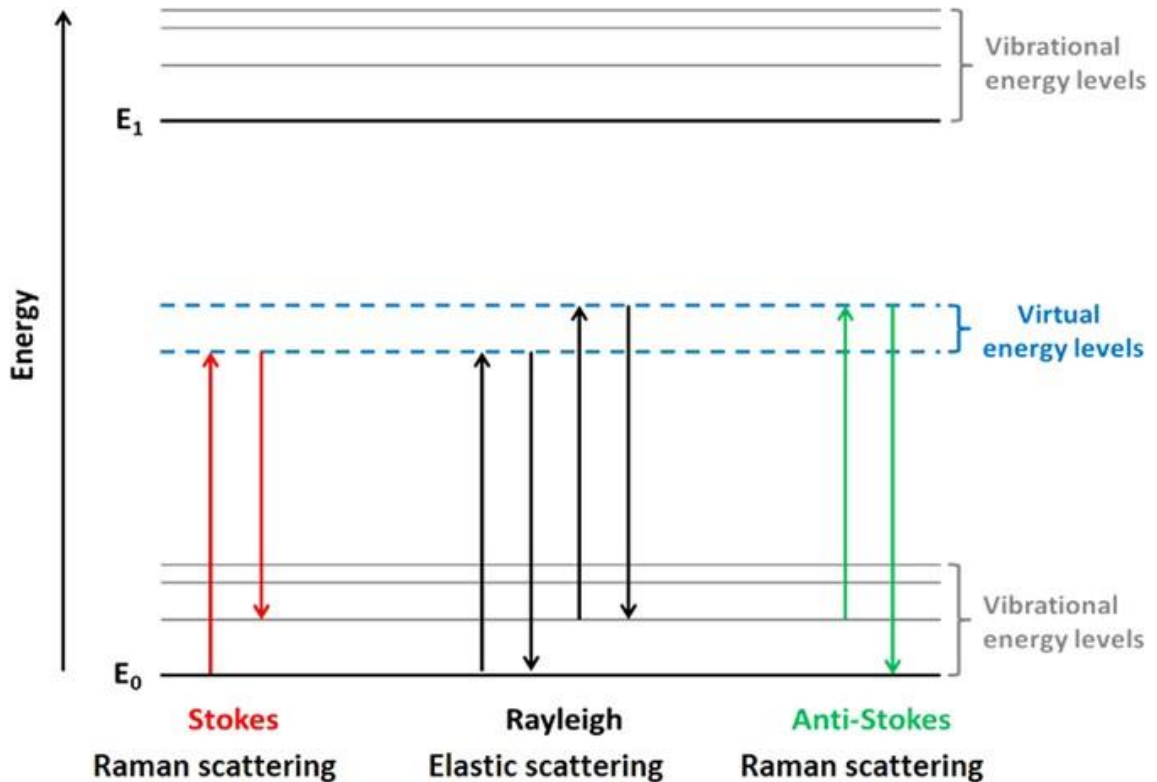
Figure 2.3 Schematic diagram of Stokes, Rayleigh and Anti-Stokes scattering[90]

2.2.4 Atomic force spectroscopy

Atomic force microscopy (AFM) is widely regarded as the most efficient and helpful microscopy technique for investigating materials at the nanoscale. As an AFM can scan not only 3D topography but also present many kinds of surface information to researchers and technologists. It is efficient that AFM can provide atomic resolution and angstrom height information pictures with minimum specimen preparation. An AFM employs an extremely sharp tip for scanning the surface of the sample. The cantilever deflects the surface when the tip approaches the surface due to the close-range, attractive force between the surface and the tip. The cantilever deflects towards the surface when the tip

approaches the material due to the close-range, attractive force between the surface of the sample and the AFM tip. Nevertheless, when the cantilever moves closer to the material surface, the tip comes into contact with the surface, resulting in rising repelling force takes over. Contact mode and tapping (also called dynamic) mode are the two most common types of AFM operating modes. AFM is based on the principle that a nanoscale tip is connected to a tiny cantilever, which acts as a spring. When the tip contacts with the sample surface, the bending of cantilever is measured by a laser diode and a split photodetector. The interaction force between tip and sample is indicated by the bending. The tip is pressed into the surface in contact mode, and an electrical feedback loop monitors the interaction force between tip and sample throughout raster scanning to maintain the deflection constant. In order to protect the surface and the tip from damage, tapping mode restricts the amount of contact between them. The cantilever is designed to vibrate near the frequency of its resonance in this mode. The tip swings up and down, which is known as a sinusoidal motion. As it gets closer to the sample, attractive or repulsive interactions slow the motion down. In a similar way to contact mode, a feedback loop is utilized to maintain the amplitude of the tapping action steady rather than the quasistatic deflection. The topography of the sample is attributed line by line in this method.
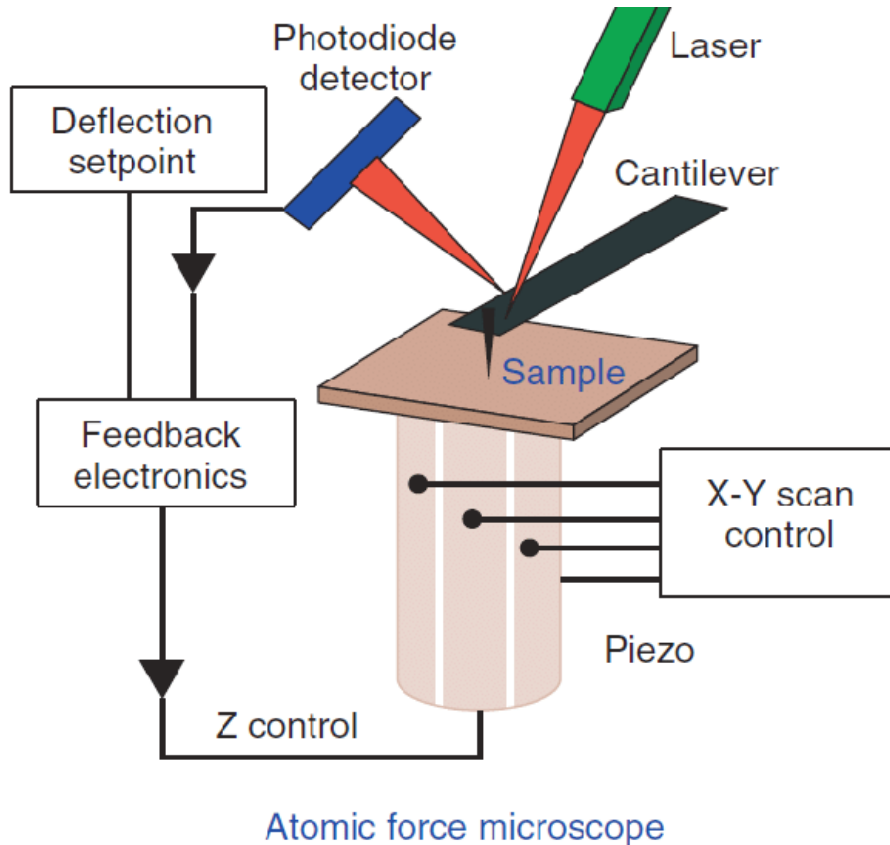
Figure 2.5 Schematic illustration of set up inside an AFM [91]

2.2.5 UV-vis absorption and photocurrent spectrum measurement systems

UV-Vis Spectroscopy is an investigation method, which compares the amount of distinct wavelengths of UV or visible light absorbed or transmitted by a specimen to a reference or blank sample. The absorption of ultraviolet or visible light by chemical substances, resulting in the formation of different spectra, is the basis of UV-vis spectroscopy. The interaction between light and matter is the fundamental principle of spectroscopy. Excitation and de-excitation occur as the matter absorbs light, leading to the formation of

a spectrum. When matter absorbs the incident radiation, the electrons excitation takes place, which lead to the movement from a ground state to an excited state. It is worth noting that the difference between ground and excited states is always equivalent to the amount of light it absorbs. The Beer-Lambert law states that when an incident monochromatic light beam on a specimen, the decline rate of the incident beam along the specimen is proportional to the concentration of the absorbing substance in the specimen and the incident light intensity. During the experiments, UV-vis measurement system (SHIMADZU) was used to obtain the absorption spectra with incident light travel through α-In_2Se_3, WSe_2 and their heterojunction. For the photocurrent spectra, PL measurement system (FLS920) is used as light source providing incident light in different wavelength, whereas the device is connected to a Keithley 4200 collecting the photocurrent outcomes.

2.2.6 X-ray Photoelectron Spectroscopy

Photoelectron spectroscopy is an investigative method that uses the photoelectric effect to measure the energy of photoelectrons released from a sample's surface in order to explore the chemical composition of materials and/or identify molecular bonding. For various measurement application scenarios, X-ray and ultraviolet (UV) radiation are used as excitation sources. High vacuum is necessary for measurements in many forms of photoelectron spectroscopy to prevent scattering between the photoelectrons and surroundings.

X-ray photoelectron spectroscopy (XPS) is a quantitative method for identifying the elemental composition and empirical formula of a material as well as the ratio and oxidation state of the elements present. XPS spectra are generated by irradiating a solid

surface with an X-ray beam of 10 nm penetration depth while analyzing the kinetic energy of electrons emitted from the material surface under investigation. Due to the high energy of the X-ray photons, the excited electrons can escape from the atoms and become photoelectrons with a specific kinetic energy. Detecting ejected electrons along a range of electron kinetic energies forms a photoelectron spectrum. An electron might be ejected while an atom or molecule absorbs an X-ray photon. The kinetic energy (E_k) is determined by the photon energy (hv) and the binding energy (E_B), which is known as the energy required to remove the electron away from the surface. After analyzing the kinetic energy of the released electrons, we can not only identify the chemical states of the elements near the surface but also determine the binding energy of electrons. The binding energy is determined by a number of variables, including from which element and orbital the electron is emitted and the chemical environment inside the atom. The Nexsa XPS system was utilized to obtain XPS spectra in this work.
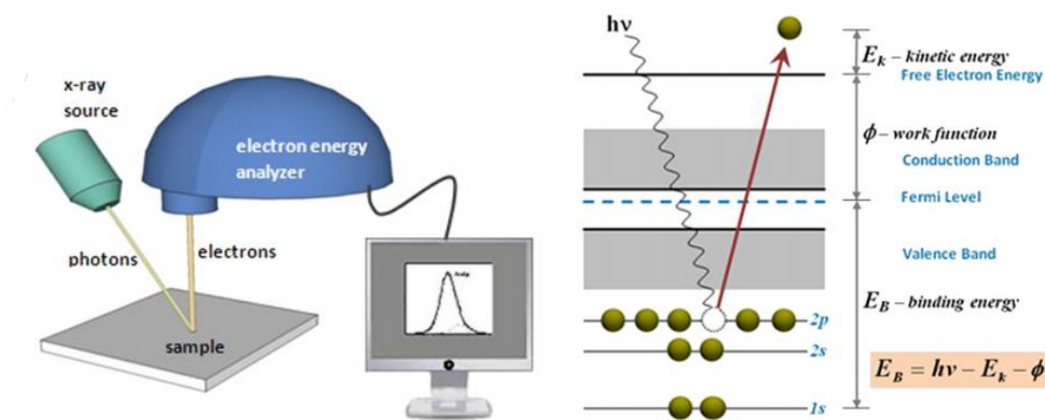
Figure 2.6 Schematic diagram of the XPS setup (left) and the energetic of the

photoemission process (right) [92]

2.3 Fabrication of 2D devices

Standard photolithography (Suss MA6 Aligner) was used to pre-patterned the electrodes onto the PET substrate, followed by evaporating the Cr/Au electrodes by the electron-beam evaporation. The mechanically exfoliated samples are then dry transferred onto the pre-fabricated PET substrate.

2.3.1 Photolithography

Over the last 30 years, photolithography has been one of the commonly utilized techniques for patterning polymers, which is the method used to transfer the pattern from a mask to the substrate surface. Patterns are created by exposing a light sensitive photoresist covered substrate to photo-irradiation through a patterned mask and then removing a specified part of the film by dissolving in a suitable solvent. Photolithography makes it very simple to build structures of any desired shape quickly and consistently at the micron and even nanoscale that has been widely used in many fields, including semiconductor Integrated Circuits (IC) fabrication, sensors in micro-electromechanical systems (MEMS) and so on.

The next part depicts the detailed photolithography steps and parameters that we employed in our tests. The substrate was first placed on the spinner, and suction was applied using a vacuum pump. The chemical AZ5214 was applied to the substrate as a positive photoresist, resulting in a polarity picture on the wafer that is identical to that on the mask. In order to obtain higher resolution, positive resist was used. Bubbles must be prevented throughout the dripping process, and the resist applied must cover the whole substrate. The spin coater's speed was then adjusted to reach 500 rpm in 5s and stay there for another 5s, then

4000rpm in 5s and stay there for another 30s, as the thickness of the photoresist that is applied to the substrate should not exceed 1 μm. Then, using the knobs on both sides of the aligner, position the mask on top of the PET and align it in the desired direction using the microscope. After alignment, the UV light shines through the quatz mask onto the substrate for 7s, enabling the patterns on the mask to be constructed on the substrate. The AZ300MIF developer was then applied to remove a certain part of the photoresist and generate designed patterns by immersing the sample in the developer for approximately 20 seconds and afterwards washing with DI water.
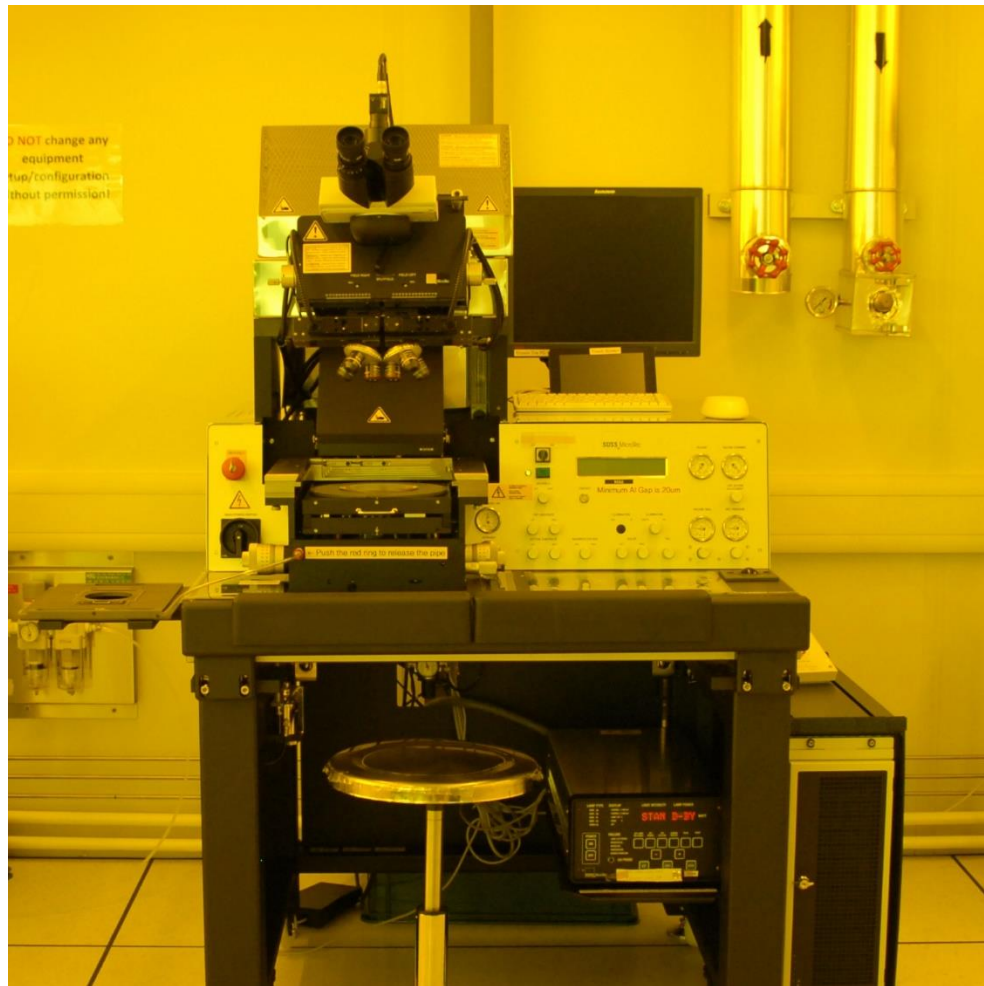
Figure 2.7 SUSS MA6 Mask Aligner

2.3.2 Electron beam metal evaporation and lift off

Electron Beam (E-beam) Evaporation is a kind of Physical Vapor Deposition (PVD) where the target material used is evaporated and converted to a gaseous state for deposition on the to be coated material by an electron beam through blasting with a charged tungsten filament. In a high vacuum chamber, these vapor phase atoms or molecules subsequently precipitate, and a thin film coating is generated on the substrate. It enables direct energy transmission from the Electron Beam to the target material to be evaporated, providing a suitable mechanism for metals with high melting points. Electron Beam Evaporation provides substantially faster deposition rates ranging from 0.1 nm to 100 nm per minute, leading to increased density film coatings with improved adhesion to the substrate. In addition, comparing to other PVD processes, E-Beam Evaporation has a very high material utilization efficiency, which reduces the costs. Rather than heating the whole crucible, E-beam system only heats the target source, leading to less crucible contamination. With focusing the energy on the target instead of the whole vacuum chamber, the potential of heat damage to the substrate is reduced. A multiple crucible E-Beam evaporator can apply several layers of coating from various target materials without breaking the vacuum, making it adaptable to a number of lift-off masking processes.

Denton E-beam evaporation was used to produce a pair of 10 nm/50 nm Ti/Au electrodes after photolithography. A lift-off procedure is necessary after an e-beam evaporation to eliminate the excess Ti/Au film other than the electrodes on the substrate. The Ti/Au films normally fall off after the substrate submerging in acetone for a few hours. When this treatment does not work, we might heat up the solution or extend the dip-in time.

Ultrasonic is usually the least preferred choice since it might damage the interface between

the Ti/Au electrode and the sample flakes.

Figure 2.8 Denton Explorer E-beam deposition system

2.3.3 Dry transfer

To construct the vdW contact between 2D materials, a dry transfer approach was used.

Multilayer α-In_2Se_3 and WSe_2 flakes were obtained from high quality crystal (HQ

graphene) onto the SiO_2/Si substrates through mechanical exfoliation. The polyvinyl alcohol (PVA) films used during the process were made by drying a 4% PVA aqueous solution for two days on a CD for 48 hours. The flakes were mechanically picked up from the SiO_2/Si substrate using the PVA film. The sample flakes and the PVA film were then attached to a polydimethylsiloxane (PDMS) stamp. To prevent strong interaction between the PVA and the 2D flakes, the temperature during the picking up operation was adjusted to 60 ℃ for 5 minutes. High drying temperatures cause considerable interactions between the PVA film and the 2D materials, resulting in a poor yield rate. The 2D material flakes are oriented onto the electrodes using a microscope fitted with a micro-manipulator after the 2D material flakes adhered to the PVA film. To construct good connections between materials and electrodes, the heterostructure photodetector was warmed to 60 ℃ for 5 minutes after alignment. Lastly, to prevent 2D materials from moving during bending conditions, a layer of poly (methyl methacrylate) (PMMA) was spin-coated above the heterostructure surface.

2.4 Electronic and photoelectronic characterization of devices

All electronic and photoelectronic tests are performed at room temperature. The illumination source is a red light emitting diode (LED) with a wavelength of about 620nm.
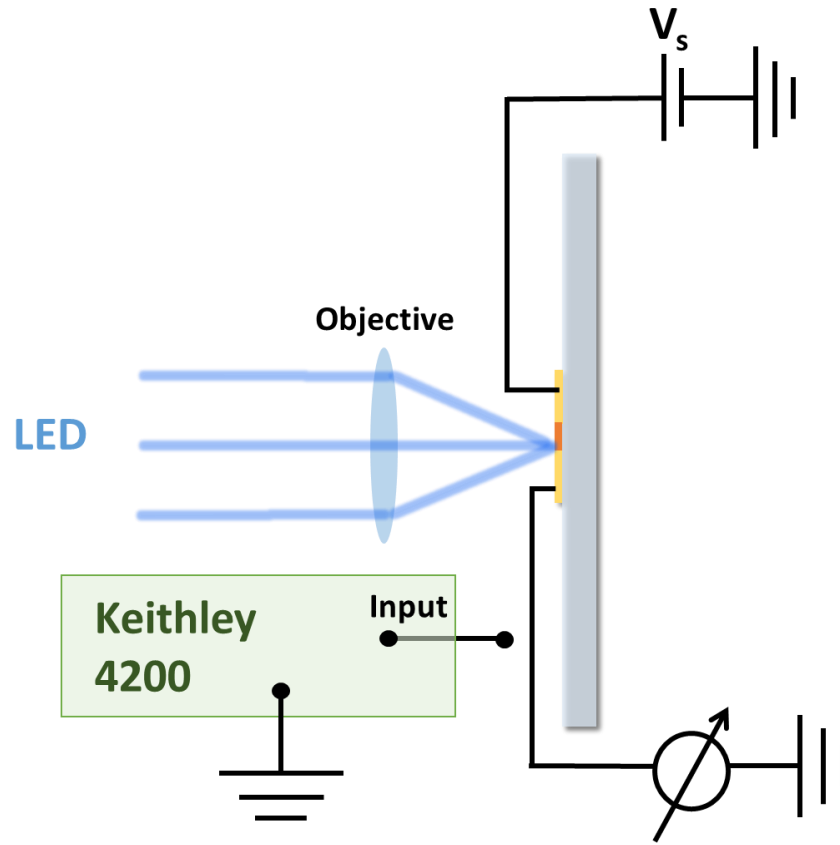
Figure 2.9 Schematic illustration of the α-In$_2$Se$_3$/WSe$_2$ heterojunction photodetector

under light illumination and strain-free condition.

The optical power of the 620nm red LED was measured with the laser power meter (sanwa). The intensity of the LED can be calculated by measured power/area of light sensor window power. Power and intensity dependence of applied voltage is displaced In Table 1.

Table.1 Incident light power and intensity under different applied voltage

Voltage (V)	Power (μW)	Intensity (μW/cm^2)
1.58	0.02	0.069

1.66	0.09	0.318
1.74	2.91	10.3
1.80	21.8	77.1
1.96	221	782

To control the strain applied to the device, a self-made two-point bending apparatus is employed. The Keithley 4200, which links to a probe station with a semiconductor analyzer, is used to measure and gather the electrical characterisation.
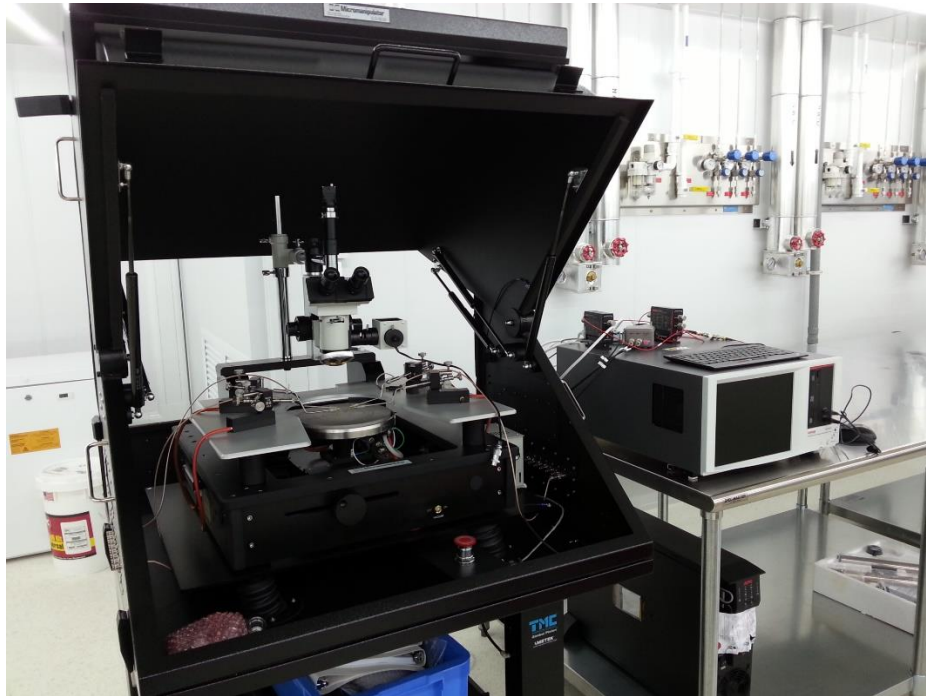
Figure 2.10 Probe Station with semiconductor parameter analyzer

For the purpose of calculating the amount of applied strain, the device under bending is modeled as a circular arc as shown in schematic diagram.
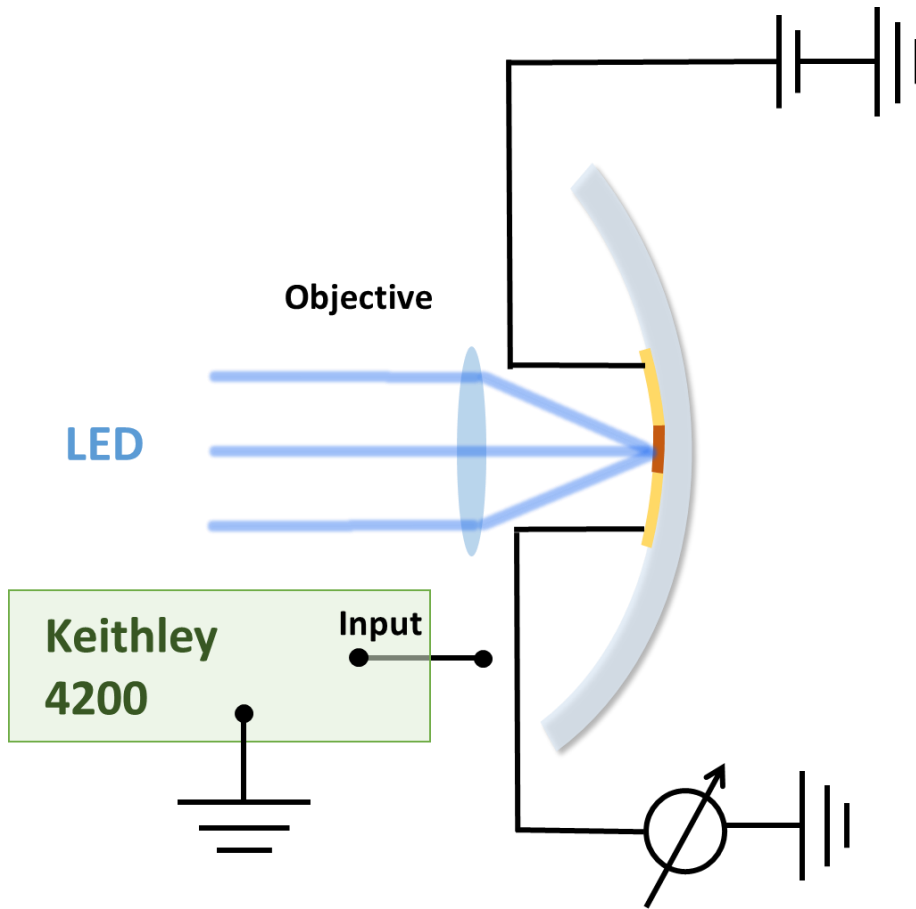
Figure 2.11 Schematic illustration of the α-In$_2$Se$_3$/WSe$_2$ heterojunction photodetector under light illumination and compressive strain condition.

Chapter 3 Fabrication and Characterization of α-In₂Se₃ and WSe₂

3.1 Fabrication of the p-n junction

The first monolayer graphene was obtained in 2004 using the mechanical exfoliation process, and the biggest cleaved graphene to date is on the order of millimetres. This technique may also be used to prepare a variety of other 2D materials, such as TMDCs. This method may also be used to prepare a variety of other 2D materials, such as TMDCs. Moreover, graphene and other 2D materials may be obtained on desired substrates using this approach. Dry transfer produces the cleanest and highest-quality samples, making it the ideal option for researching novel fundamental physics and device concepts. Mechanical exfoliation was utilized to prepare the high-quality multilayer α-In$_2$Se$_3$ and WSe$_2$ flakes used in this thesis. The optical picture of the α-In$_2$Se$_3$ and WSe$_2$ heterostructure fabricated by dry transfer method with accurate alignment of the flakes onto a PET substrate with Ti/Au (10nm/50nm) pre-fabricated electrodes is shown in Figure 3.1. The PET substrate was chosen because of its high transparency and solvent resistance. Furthermore, PET has a relatively high Young's modulus, ensuring that the induced-strain is readily transmitted to the 2D nanoflakes during bending. The dry transfer method was used to avoid the use of a strong acid or alkali solution, allowing the optoelectronic characteristics of materials to be preserved without significant degradation.
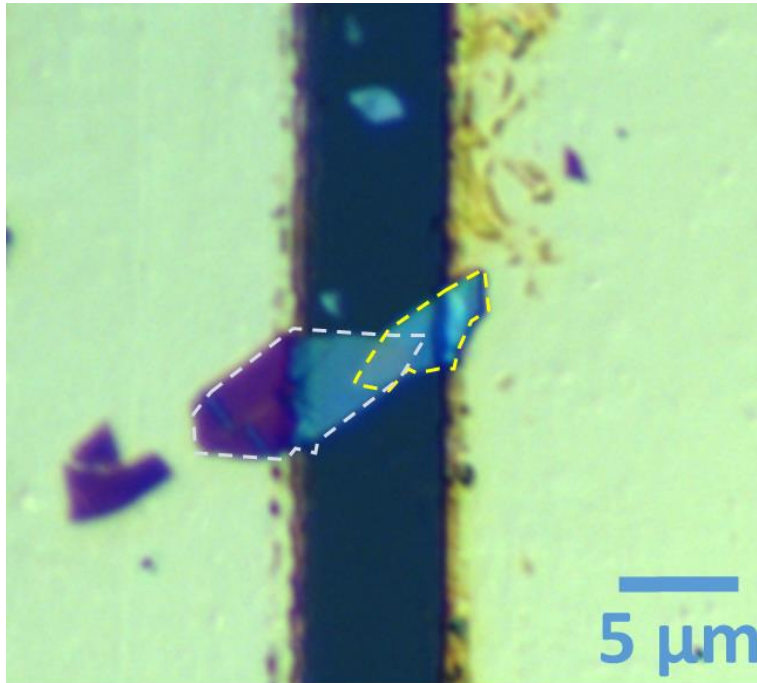
Figure 3.1 Microscopy image of the 2D material flakes and electrodes constructing the

photodetector.[93]

3.2 AFM characterization

The most widely used technique for characterizing the thickness of 2D materials on silicon

wafer substrates is AFM in the AC mode (also known as tapping mode). AFM is a

necessity for studying 2D materials, as the number of layers can be precisely determined

by this approach. AFM scanning can also be used to provide surface conditions. The

topological quality is examined and the step height between substrate and sample is

measured during experiments using AC mode AFM. The smooth and clean surface of α-

In_2Se_3 and WSe_2 observed in the inset figures demonstrates that high quality of the few-

layer 2D flakes have been fabricated. Before being placed onto the PET substrate, the thickness of the 2D nanoflakes was evaluated using atomic force microscopy (AFM), as shown in Figure 3.2 and 3.3. The thicknesses of α-In_2Se_3 and WSe_2 flakes are deduced to be about 20 nm and 8 nm, respectively.
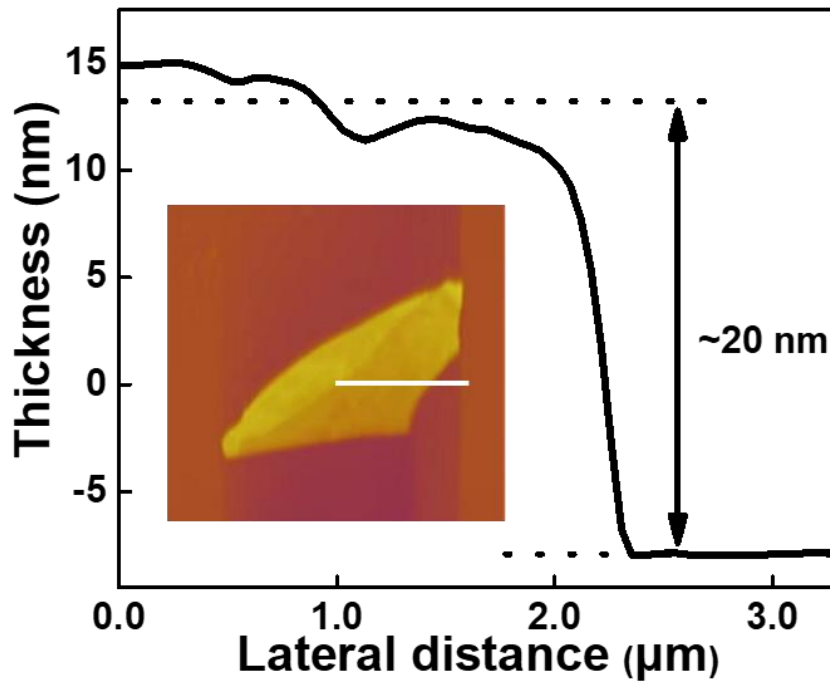
Figure 3.2 AFM height profiles of α-In_2Se_3. Inset: corresponding AFM image.
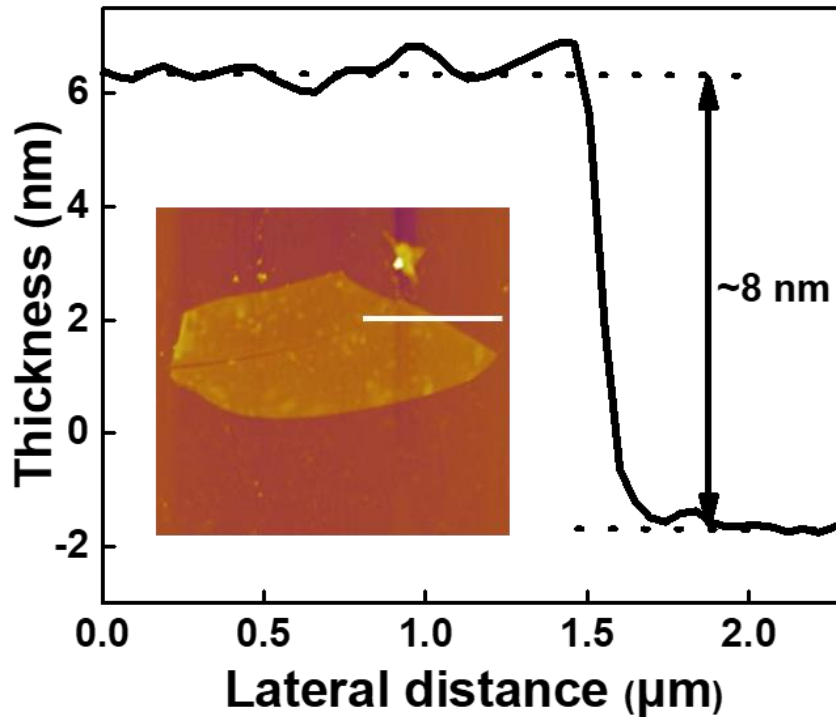
Figure 3.3 AFM height profiles of WSe$_2$. Inset: corresponding AFM image.

3.3 Raman and PL characterization

Raman spectroscopy is an extremely useful technique to identify 2D materials and compare them with their bulk states. Raman spectroscopy is an excellent method since it is not only efficient and non-destructive, but it also has a good resolution, which provides structural and electrical information, and can be used at both research and industry scales. Furthermore, the Raman shift can be used to determine the thickness of 2D flakes. We utilize Raman spectroscopy to characterize few-layer samples in our research. The multilayer WSe$_2$ and α-In$_2$Se$_3$ flakes were characterized using Raman spectroscopy, and

the Raman spectra of WSe_2 and α-In_2Se_3 are shown in Figure 3.4. The Raman peaks E, A_1 (LO+TO), A_1 (LO) and A_1 (TO) phonon modes of α-phase In_2Se_3 are located at around 88 cm^{-1} ,104 cm^{-1} 180 cm^{-1} and 195 cm^{-1}, respectively. The 248 cm^{-1}, 261 cm^{-1} and 305 cm^{-1} indicates A_{1g} mode, second order peak 2LA(M) and a combination mode of a shear and $B^1{}_{2g}$ modes of WSe_2 are also recognized.
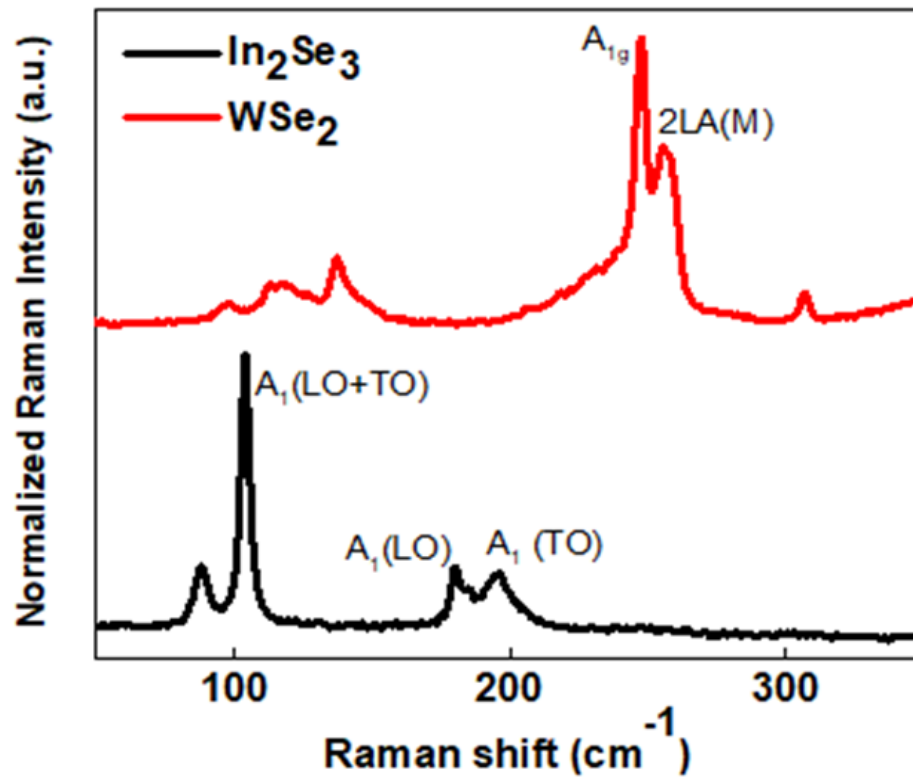
Figure 3.4 Raman spectra of α-In_2Se_3 and WSe_2 flakes.

Photoluminescence (PL) is a non-destructive, quick, and contactless method for identifying the material electronic structure. It is a useful technique for analyzing the band gap transition in 2D semiconductors dependent on the number of layers. Taking the band gap in MoS_2 (a typical TMDC material) as an example, the transitions from direct bandgap

in monolayer to indirect bandgap in bilayer and above can be clearly identified using PL. Figure 3.5 depicts the photoluminescence (PL) emission peaks position at 1.44 and 1.64 eV corresponding to α-In_2Se_3 and WSe_2, which agree with previous reports. The WSe_2 and α-In_2Se_3flakes employed in this study can be confirmed with high quality using Raman and PL spectra, we can deduce that the flakes used in this work are in high quality with superior optical properties which are suitable for constructing photodetecting devices.
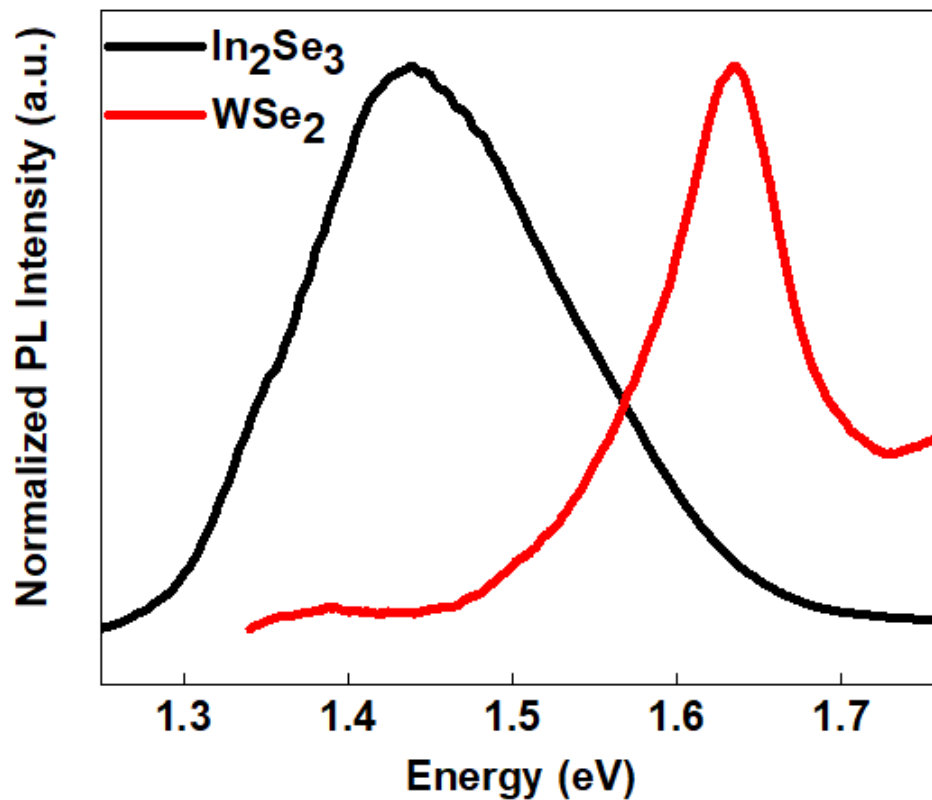
Figure 3.5 PL spectra of α-In_2Se_3 and WSe_2 flakes.

3.4 Photocurrent and absorption characterization

The light response of p-type WSe_2 and n-type $\alpha\text{-}In_2Se_3$ nanoflakes in visible light range were plotted in Figure 3.6a and 3.6b. The photocurrent spectra also show a similar trend as the absorption spectra of single materials and heterostructure based devices.
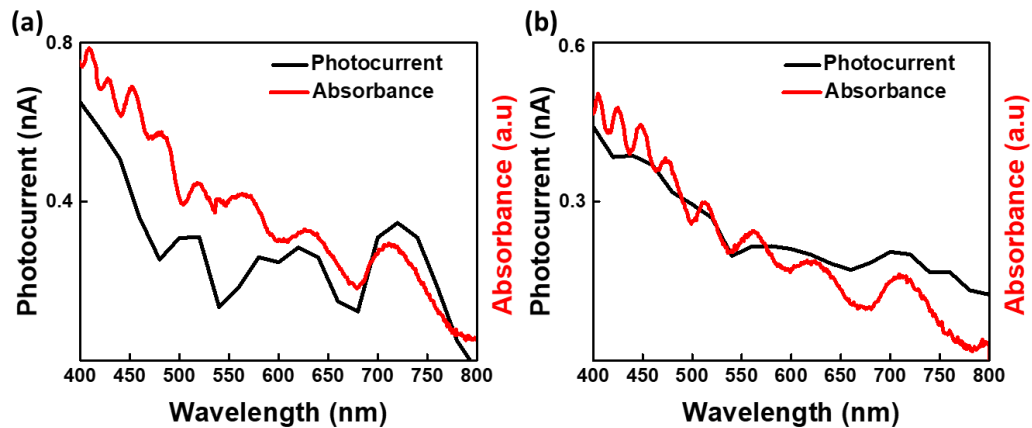
Figure 3.6 Photocurrent and absorption spectra with light incident through a) 23 nm thick $\alpha\text{-}In_2Se_3$ b) 9 nm thick WSe_2

Furthermore, since the magnitude of the photocurrent induced from our heterojunction device in this work is sufficiently higher than that measured from the devices based on single materials over around ten times, we believe that the photocurrent is largely enhanced by improving the separation efficiency of electron-hole pairs near the heterojunction interface (presented in Figure 3.7).
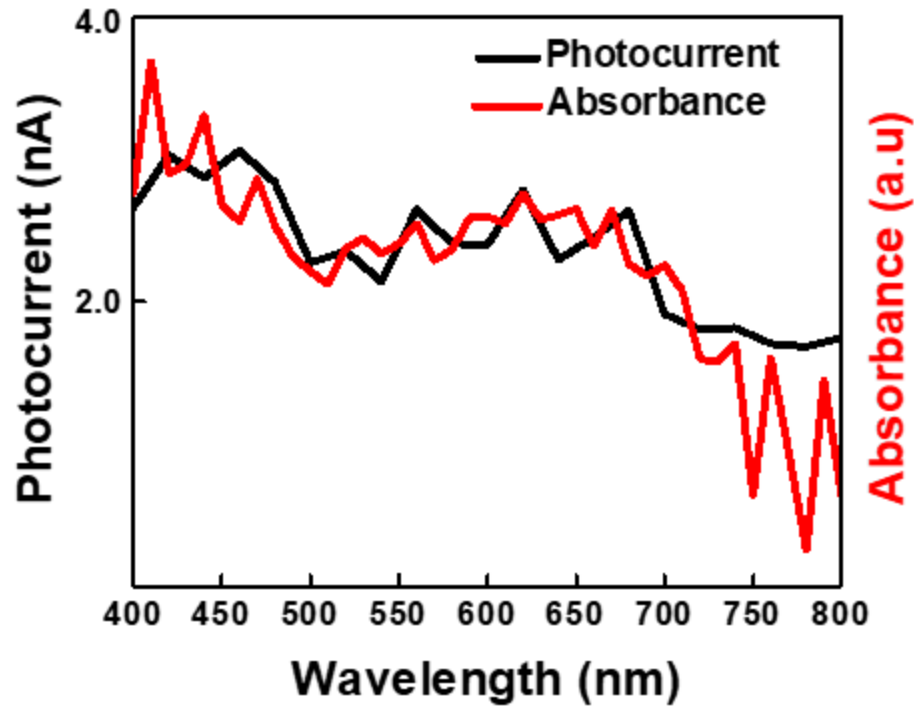
Figure 3.7 Photocurrent and absorption spectra with light incident through the α-

In$_2$Se$_3$/WSe$_2$ heterojunction

3.5 XRD characterization

As illustrated in Figure 3.8, the typical XRD pattern is used to indicate the internal structure of α-In$_2$Se$_3$ and WSe$_2$. For α-In$_2$Se$_3$ nanocrystals, the (0004) crystal plane has strong reflection peaks at 18.47°. The mono-hexagonal phase of as-prepared α-In$_2$Se$_3$ crystal was verified by the peaks (0002), (0006), (0008), (0010), (0012), and (0014). For WSe$_2$, (0002) crystal plane displays significant reflection peaks at 13.66°. Peaks (0006), (0008) and (0010) confirmed the mono-hexagonal phase of the WSe$_2$ crystal.
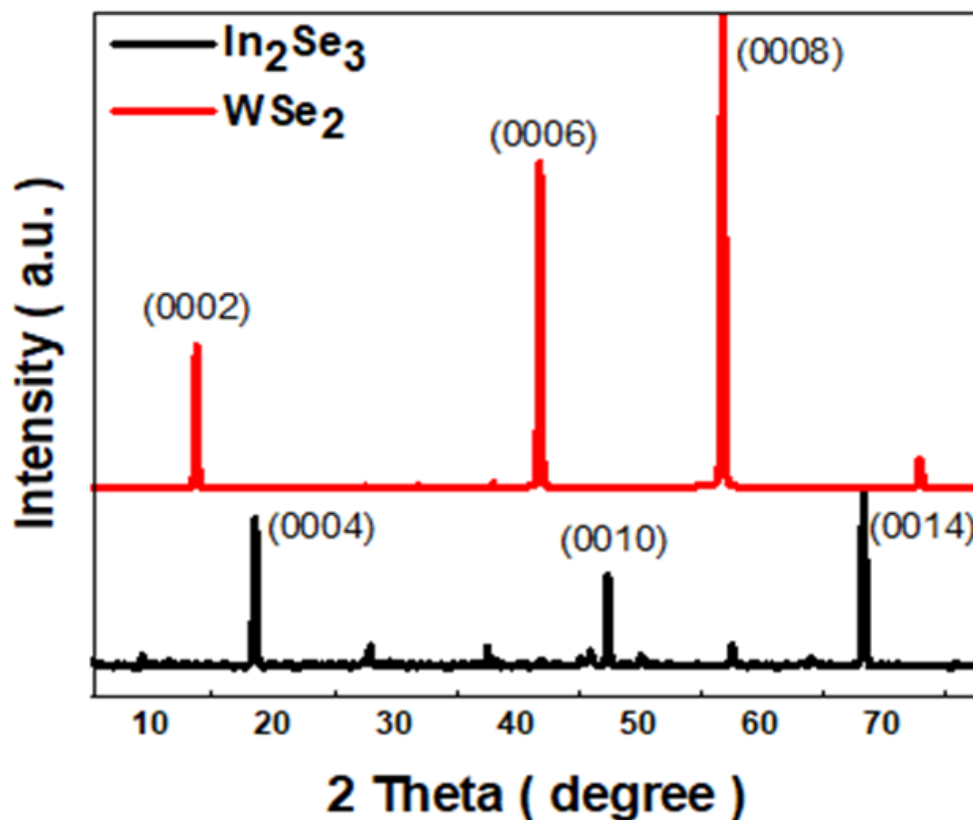
Figure 3.8 XRD spectra of WSe₂ and α-In₂Se₃

3.6 XPS Characterization

XPS measurement was carried out to further confirm the elemental composition of the mechanically exfoliated α-In₂Se₃ and WSe₂ flakes. Strong XPS doublets can be observed at 445.2 and 452.7 eV correspond to the In 3d $_{3/2}$, and In 3d $_{5/2}$ core level orbitals, respectively. As presented in Figure 3.9, reflection peaks of Se 3p $_{3/2}$ and Se 3p $_{5/2}$ are displayed as the pair peak at 54.1 eV and 55.2 eV respectively, demonstrating the chemical composition of the α-In₂Se₃ flakes.
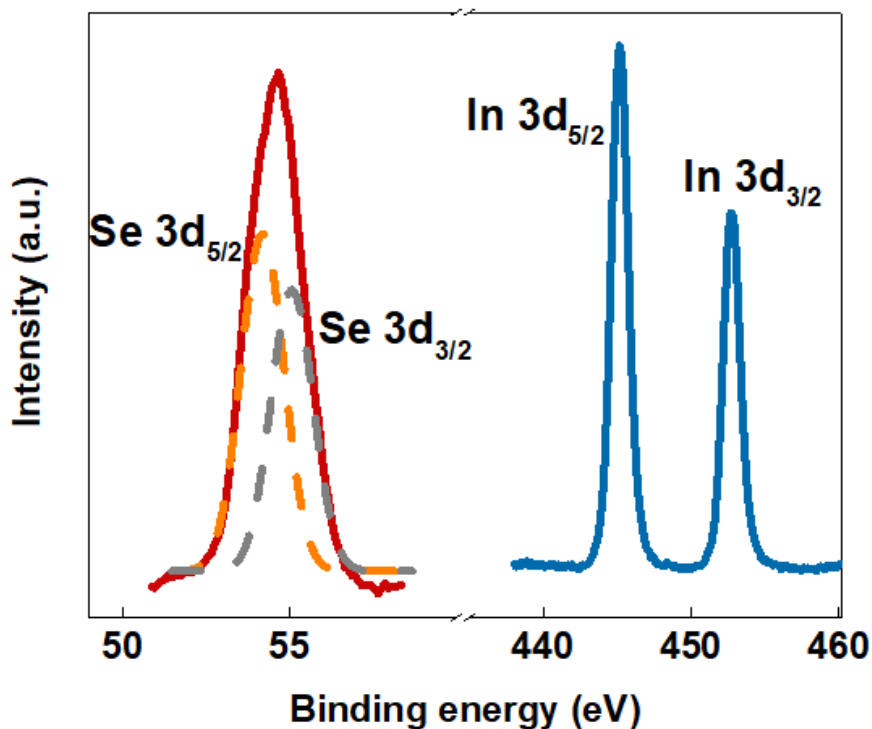
Figure 3.9 XPS spectrum of α-In$_2$Se$_3$ flakes

Figure 3.10 presents the XPS spectrum of WSe$_2$ nanoflakes on W4f and Se 3d bending energy regions. Three main peaks can be observed on the W 4f spectrum, the two sharp peaks located at 32.5 eV and 34.6 eV attribute to W 4f $_{7/2}$ and W 4f $_{5/2}$ respectively and the broad low peak around 38.1 eV attributed to the W 5P $_{3/2}$. For Se 3d, the two main doublets located at 54.8 eV and 55.6 eV correspond to the presence of Se 3p $_{5/2}$ and 3p $_{3/2}$, respectively. Both XPS spectra 2D have similar results reported in the literature before, indicating the quality of flakes are relatively good.
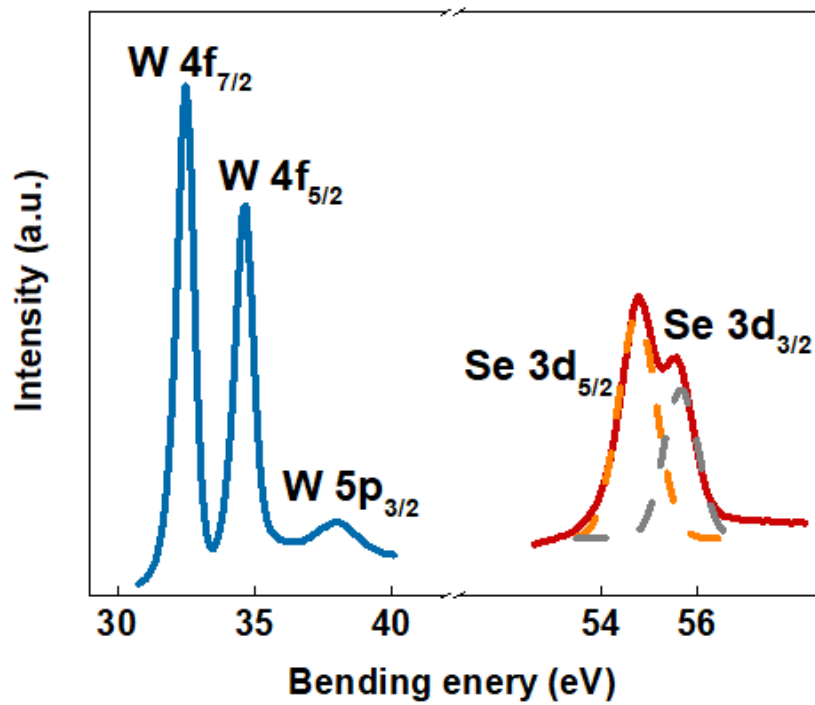
Figure 3.10 XPS spectrum of WSe₂ flakes

Chapter 4 Flexible photodetectors based on In₂Se₃/WSe₂ vdW heterostructure

4.1 I-V characterization of In₂Se₃/WSe₂ photodetector

The I-V characteristics of the heterojunction were investigated under various situations in order to investigate the performance of the heterostructure and the charge transfer characteristics between WSe_2 and α-In_2Se_3. The piezo-response of the device was measured using uniaxial strains with varying curvatures.
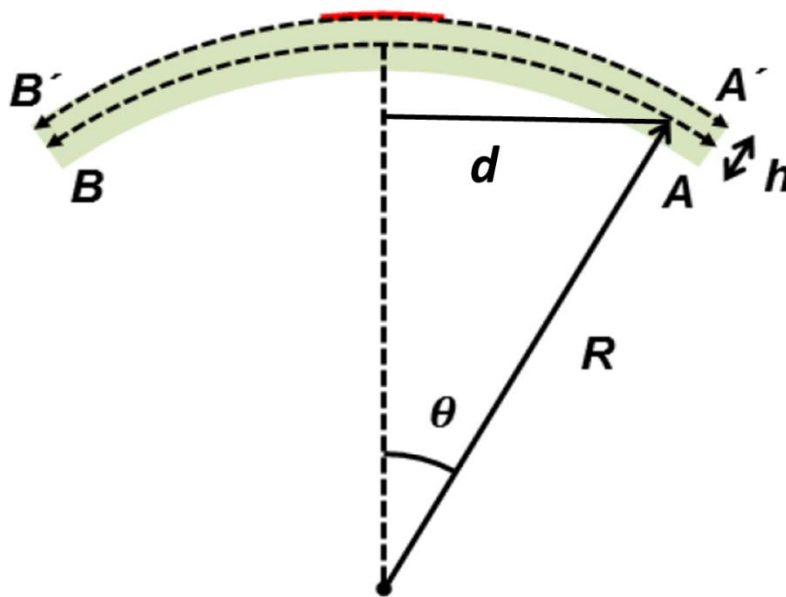
Figure 4.1 Geometrical illustration of bending In_2Se_3 photodetector [94]

As the In_2Se_3 flake was located on a PET substrate, which is extremely thin comparing with the thickness of substrate. Also, a layer of PMMA was spin-coated above the heterostructure surface to prevent 2D components from migrating during bending circumstances. We can assume that the strain applied to flake was almost identical to the strain at the outer surface of the PET substrate and can be obtained using the fundamental relation

$$\varepsilon = \frac{A'B' - AB}{AB}$$ Equation 4.1

where ε is the strain, AB is the outer surface of PET before bending and A'B' after bending. Equations can be constructed in order to solve relationship between movement of substrate and R (radius of curvature).

Based on the equation used to calculate arc length, we can deduce that

$$2\theta R = L$$ Equation 4.2

where L is the original length of PET.

$$2d = 2R \sin \theta$$ Equation 4.3

where $d = (L - movement)/2$ Equation 4.4

By combining Equation 4.2 and 4.3, we can obtain that

$$d = R \sin \frac{L}{2R}$$ Equation 4.5

In this case, length of PET substrate is 1.9cm. R can be deduced at different movement with function shown above.

With knowing amount of substrate moved during process of applying tensile strain, we can deduce the radius of curvature:

$$AB = R \cdot 2\theta \hspace{4cm} \text{Equation } 4.6$$

$$A'B' = \left(r + \left(\frac{h}{2}\right)\right) \cdot 2\theta \hspace{3cm} \text{Equation } 4.7$$

where h is the thickness of the PET substrate

Substituting AB and A'B' into the Equation 4.1, we can get

$$\varepsilon = \frac{h}{2R} \hspace{4cm} \text{Equation } 4.8$$

[94]
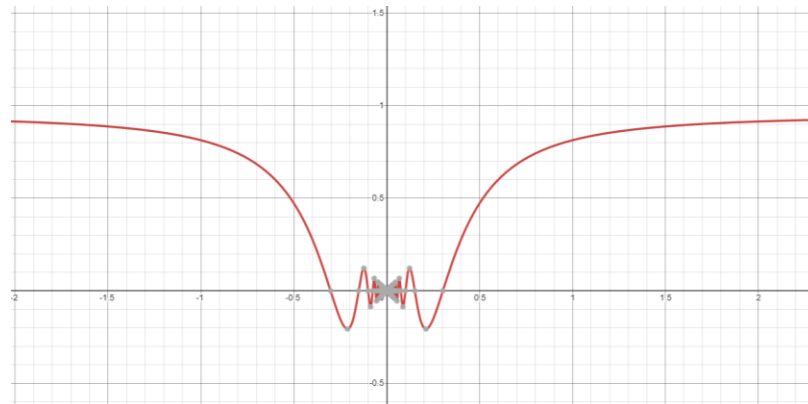
Figure 4.2 Geometrical plot of function d=Rsin(L/(2R)) where x represent R and y

represent d

In this experiment, the range of strain used is from -0.433% to 0.433%, where negative and positive sign represent for compressive and tensile strain respectively. With raising the applied tensile strain, output current gradually increases.
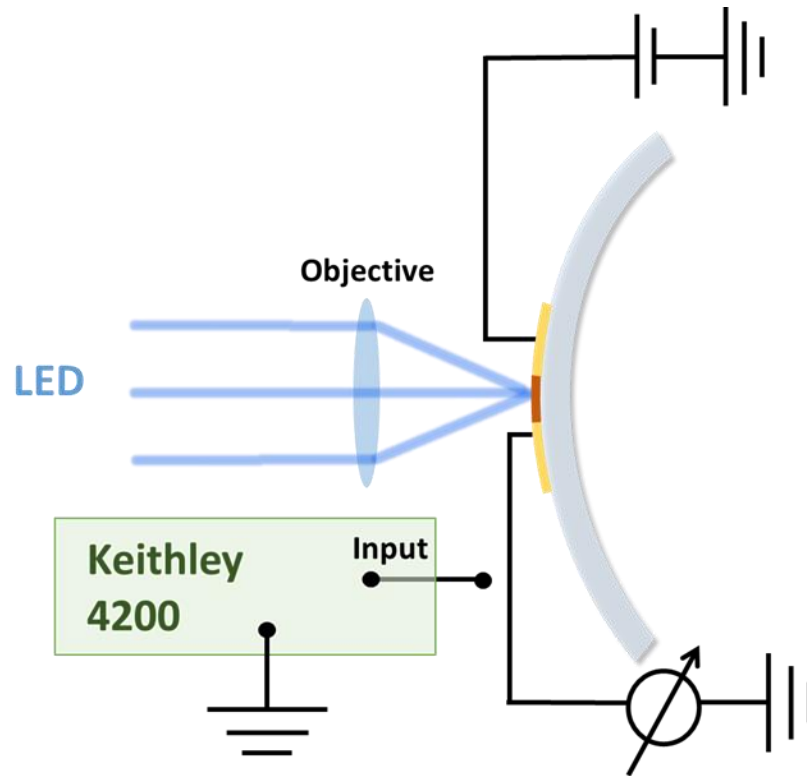
Figure 4.3 Schematic diagram of α-In₂Se₃/WSe₂ photodetector under light illumination and tensile strain condition.

The I-V characteristics of the heterojunction demonstrate the device's piezo-response under various stresses, including compressive and tensile strains ranging from 0.433 % to -0.433 %. As displayed in Figure 4.4, the dark current of the α-In$_2$Se$_3$/WSe$_2$ heterostructure device can be controlled at different strains. The I$_{dark}$ was increased from 0.54 nA to 3.61 nA under 0.433% tensile strain and decreased to 0.15 nA under 0.433% compressive strain at a bias of 2 V, demonstrating clear strain-gated vdW junction characteristics.
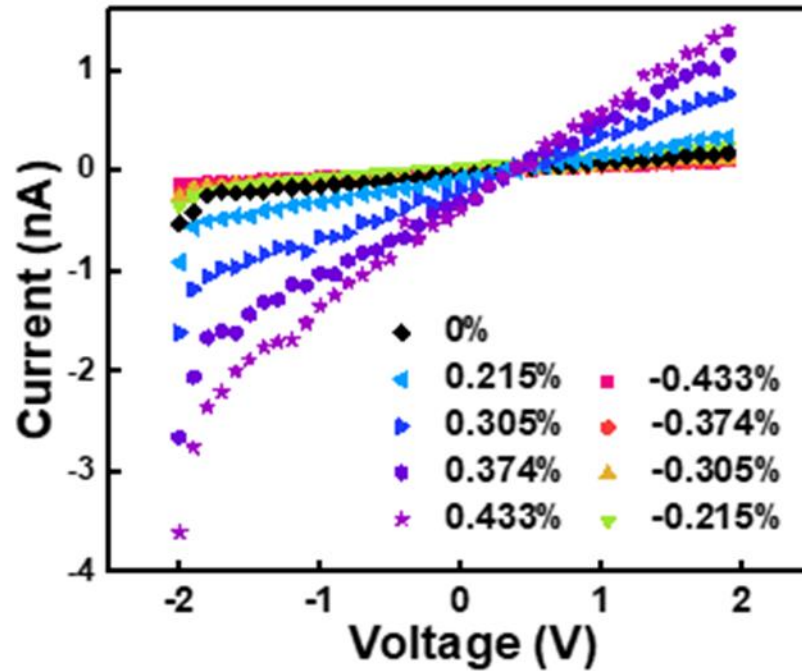
Figure 4.4 I-V curve under different strain conditions without light illumination.

Under -2 V bias and same illumination density (782 $\mu W/cm^2$), the output current increases from 27 nA to 172 nA as shown in Figure 4.5.
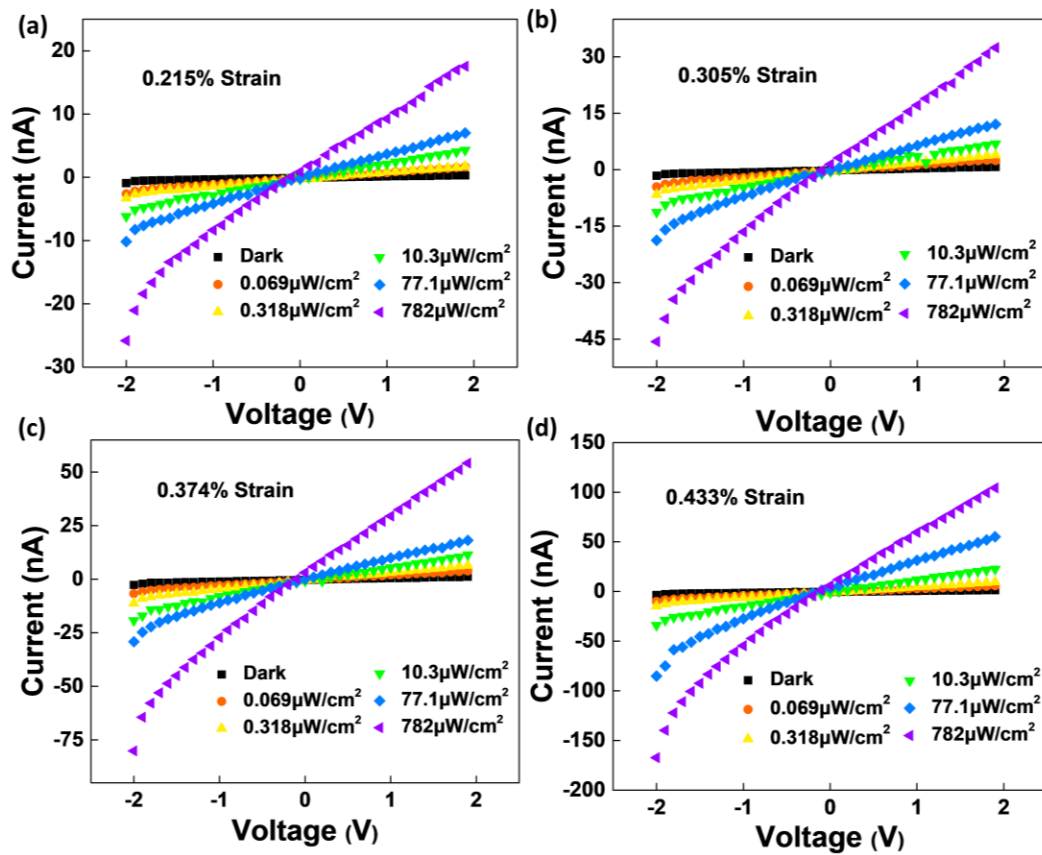
Figure 4.5 I-V curve of α-In₂Se₃/WSe₂ heterojunction photodetector applied with (a)

0.215%, (b) 0.305%, (c) 0.374% (d) 0.433% tensile stain under different light

illumination intensities.

In contrast, when compressive strain increases from 0.215% to 0.433%, the output current

decrease from 5.6 nA to 2.7 nA under -2 V bias and 782 μW/cm² intensity illumination

(presented in Figure 4.6). When applied voltage less than 0 V, relatively large current flow

through. In contrast, when applied voltage larger than 0 V, smaller output current can pass

through the device, which indicates the rectification property of the devices.
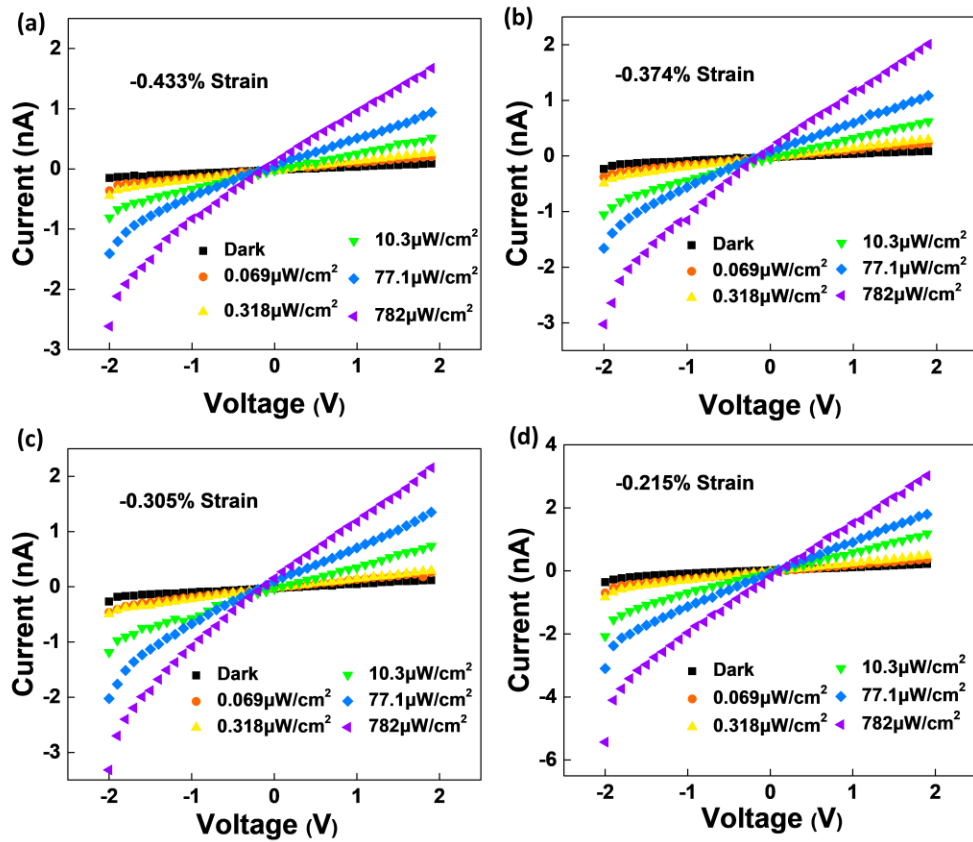
Figure 4.6 I-V curve of α-In$_2$Se$_3$/WSe$_2$ heterostructure photodetector applied with (a) -0.433%, (b) -0.374%, (c) -0.305%, (d) -0.215% compressive stain under different light illumination intensities.

A low applied voltage range was selected for the purpose of highlighting the photoresponse of the device under multiple conditions. As the rectification characteristic of the photodetector tested under narrow applied bias region (-2 V to 2 V) is not clear enough, with increasing the test region from -10 V to 10 V, good rectification properties of a p-n heterojunction device are demonstrated in Figure 4.7a. High-quality multilayer α-In$_2$Se$_3$ and WSe$_2$ flakes used in this work were mechanically exfoliated from the crystal purchased in HQ graphene, and no more doping treatments has been processed to the

nanoflakes. The asymmetric contacts and band alignment may influence the photovoltaic effect of the device. However, the *I-V* curves under different light illumination intensity without strain shows a typical P-N junction rectifying feature as plotted in Figure 4.7b, deducing that the P-N junction presents major contributions to the performance of the devices, and we would like to focus our research on the strain-regulated photoresponse of the α-In$_2$Se$_3$/WSe$_2$ heterojunction.
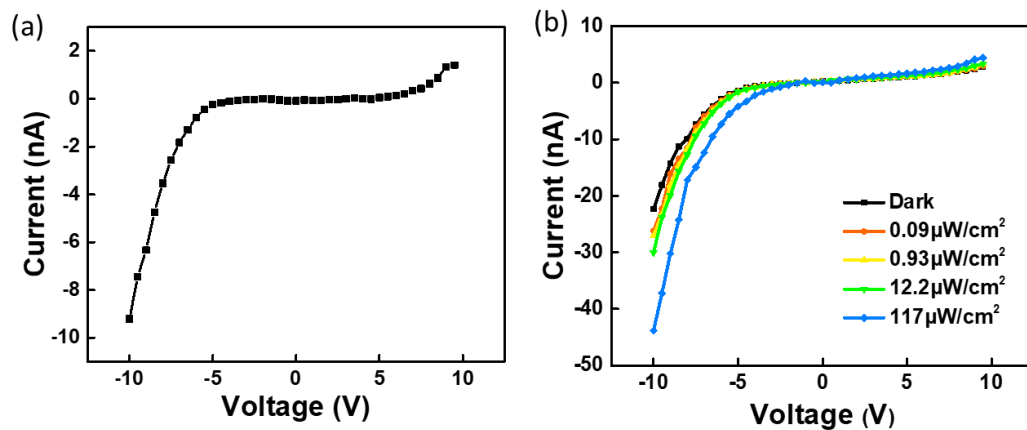
Figure 4.7 I-V curve under a) strain-free without light illumination. b) under different light illumination intensity without external strain application.

4.2 Photoresponse performance of α-In$_2$Se$_3$/WSe$_2$ photodetector

The 620 nm laser with incident power (0.069 μW/cm^2 to 782 μW/cm^2) was illuminated on the flexible photodetector to further determine the photodetection behavior of the α-

In$_2$Se$_3$/WSe$_2$ based photodetector without external strain application, as shown in Figure 4.8.
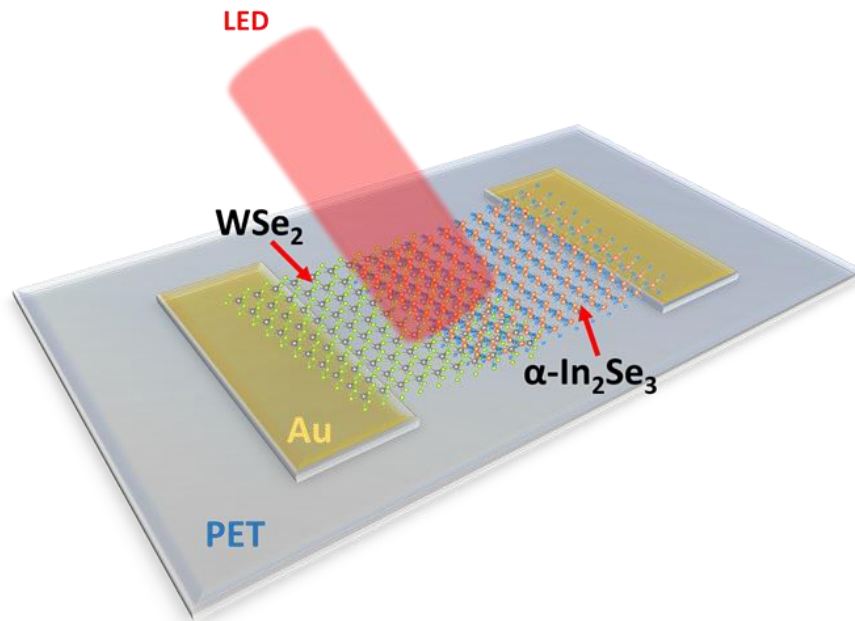
Figure 4.8 Schematic diagram of photodetector under red LED illumination.

The I-V curve under strain-free condition clearly indicates that, the light current (I_{light}) increased step-by-step from -0.54 nA to -8.33 nA with intensity increased from 0 to 782 μW/cm^2 at -2 V bias, which suggests apparent photovoltaic effect in the α-In$_2$Se$_3$/WSe$_2$ heterojunction (presented in Figure 4.9).
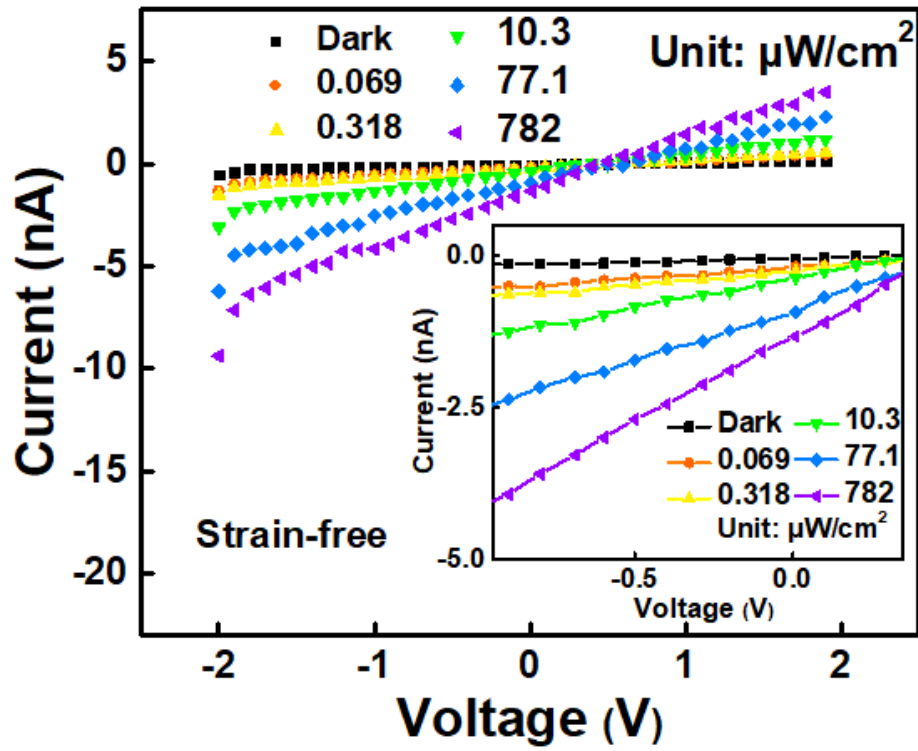
Figure 4.9 I-V curve of the α-In$_2$Se$_3$/WSe$_2$ heterojunction photodetector under different light illumination intensity without external strain application

The short-circuit current (I_{sc}) of 1.47 nA and open-circuit voltage (V_{oc}) of 0.41 V were acquired under 782 μW/cm^2 optical intensity as an illustration, presenting in Figure 4.10.
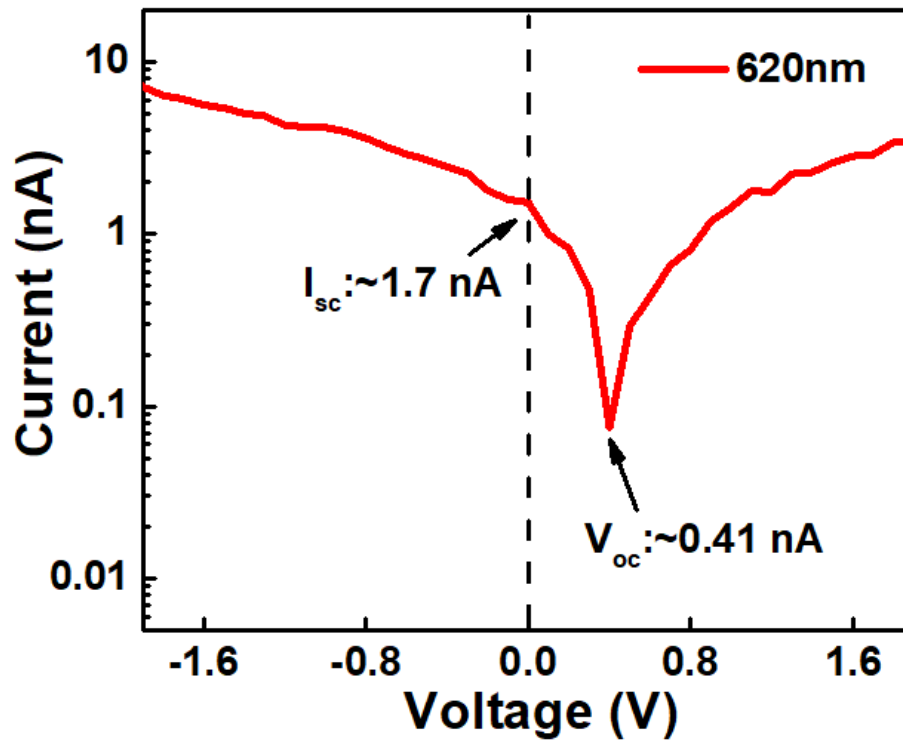
Figure 4.10 I-V curve the α-In$_2$Se$_3$/WSe$_2$ heterojunction photodetector in logarithmic

scale under strain free and 782 μW/cm^2 intensity illumination.

Figure 4.11 indicates the photocurrent ($I_{ph}=$ I$_{light}$-I$_{dark}$) increase with the illumination

intensity under -2 V bias. Besides, the curve in the inset figure indicating that it fits

perfectly to the power law, $I_{ph} \sim P^{\alpha}$, where P is the incident light optical intensity and α

is a constant determines the photoresponse of the device. The experimental data fits into

a straight line with α=0.27, indicating great absorption efficiency of the photodetector and

possible existence of photogating effect. Theoretically, photogating is the process of

modifying the conductance of a device channel by utilizing a light-induced gate field or

voltage. Localized states or hybrid structures, in this sense, is highly possible not the only

way to optimize the channel conductance and achieve photogain. Owing to the collection

of photogenerated carriers, the photoconductive effect can give fast light switching rates, whereas the photogating effect may offer high light sensitivity according to photocarrier charge trapping. Because of the scale of α is much smaller than 1, the presence of trap states and defect is fairly possible. Nevertheless, the nonlinear or power-law dependency of photocurrent on incoming light power can be a feature of photogating-dominated low-dimension photodetectors, whereas not all nonlinear or power-law correlations in low-dimension photodetectors must be ascribed to photogating effect.[95]
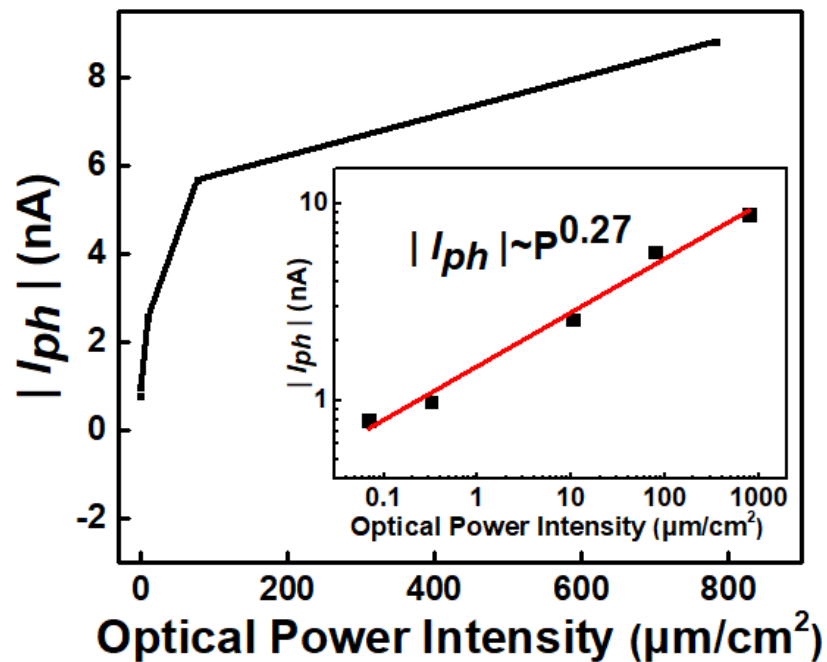
Figure 4.11 The light illumination intensity dependence of $|I_{ph}|$ in linear and logarithmic (inset) scale.

4.3 Characterization of α-In₂Se₃/WSe₂ photodetector induced by piezo-phototronic effect

In order to determine the photodetection variation induced by applying external strain, the performance of the photodetector under variable strain and illumination conditions were summarized in Figure 4.12. The I_{ph} can reach up to -164 nA under 0.433% strain and 782 µW/cm² optical intensity with -2 V bias, which is 304 times larger than the strain-free I_{dark}.
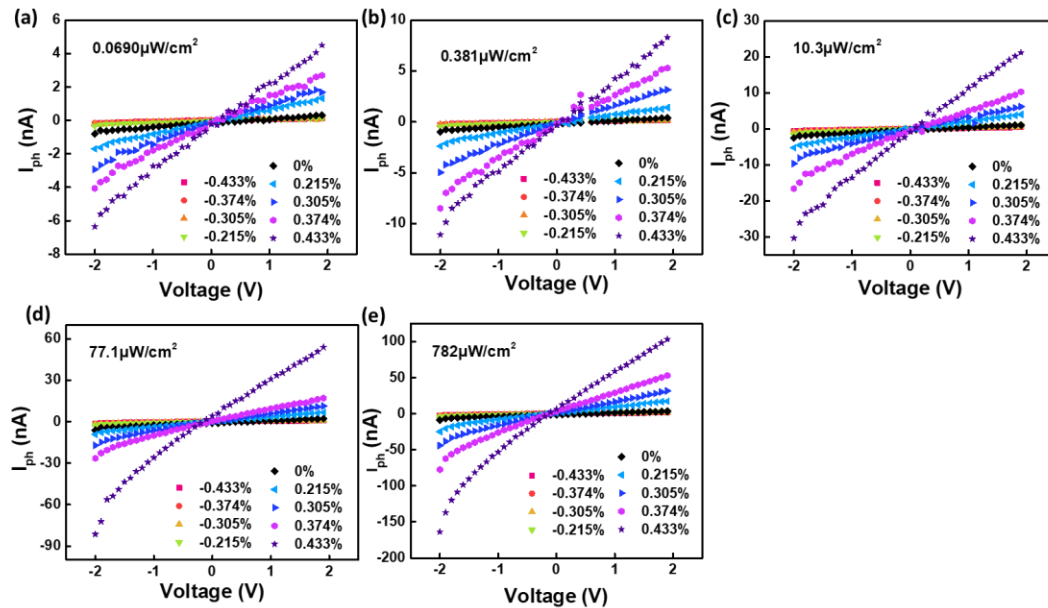
Figure 4.12 I_{ph}-V curve of α-In₂Se₃/WSe₂ heterostructure photodetector applied with various strains and (a) 0.069 (b) 0.381 (c) 10.3 (d) 77.1 (e) 782 µW/cm² light illumination.

Based on the I-V characteristics of the α-In₂Se₃/WSe₂ heterojunction photodetector, the key parameters for photodetectors such as I_{ph}, photoresponsivity (R), external quantum

efficiency (*EQE*), and detectivity (*D**) were calculated to further determine its performance. At a bias of 2 V, Figure 4.13 illustrates the I_{ph} under various light intensities and external strains. The result indicates that under equivalent light illumination intensity, the photoresponse performance of the device can be significantly influenced by the external static strain as I_{ph} increased with increasing tensile strain and decreased with increasing compressive strain. Under 0.433% tensile strain, the I_{ph} raises from 8.83 nA to 163 nA at a light intensity of 782 μW/cm^2, an almost 18 times enhancement over the strain-free condition. When piezoelectric and photoexcitation are function together, the I_{ph} can reach up to 164 nA under 782 μW/cm^2 illumination and 0.433% tensile strain and is around 210 times improvement comparing to the I_{ph} measured under strain-free and low illumination intensity (0.069 μW/cm^2) condition.
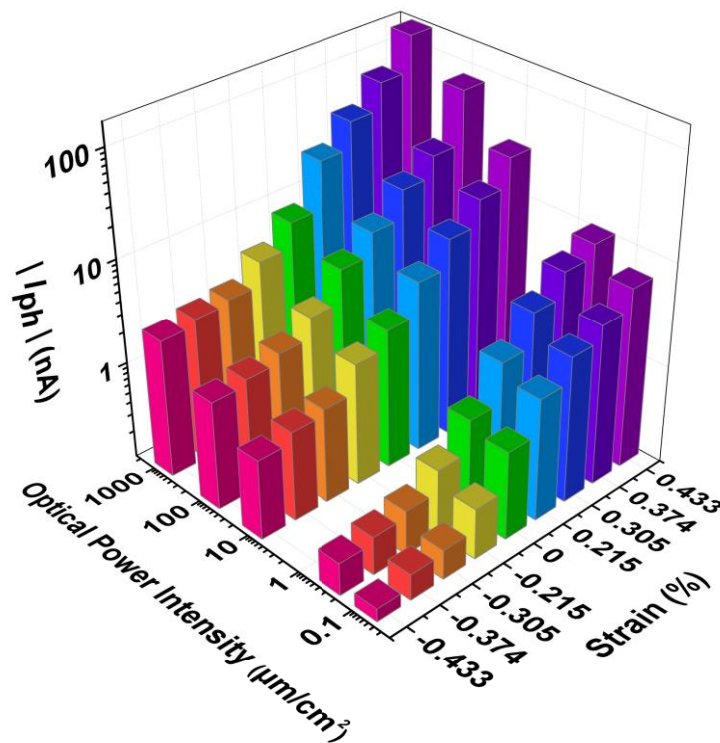
Figure 4.13 $|I_{ph}|$ under different optical power intensity and strain conditions.

In this case, the piezotronic and piezoresistive effects are two that could induce a modification in carrier transportion through the device. The outcomes convincingly demonstrate that the change of device performance by applying same amount of strain under dark and optical illumination is inequitable. When identical strain applied, the performance of the photodetector improved more under light illumination than in the dark, ruling out the photoresistive effect, which is regarded a 'volume effect' and is meant to be optical power-independent. As a result, we can conclude that the improved photodetector performance is mostly attributable to the piezo-phototronic effect.

The I_{ph} traveling through the device per effective area under per unit power of incident light is defined as R, which can be calculated using formula

$$R = I_{ph}/(PA) \hspace{3cm} \text{Equation 5.1}$$

where P is the optical intensity and A is the active illuminated area of the device. The electron number detected per incident light photon is known as *EQE*, which is calculated with the equation

$$EQE = Rhc/(e\lambda) \hspace{3cm} \text{Equation 5.2}$$

where h is the Plank constant, c is the velocity of light, e is the electron charge and λ is the wavelength of incident light. Figure 4.14 indicates that the maximum R and EQE are 4.61×10^5 A/W and $9.14 \times 10^5\%$ respectively under the 0.069 μW/cm^2 illumination intensity and 0.433% tensile strain.
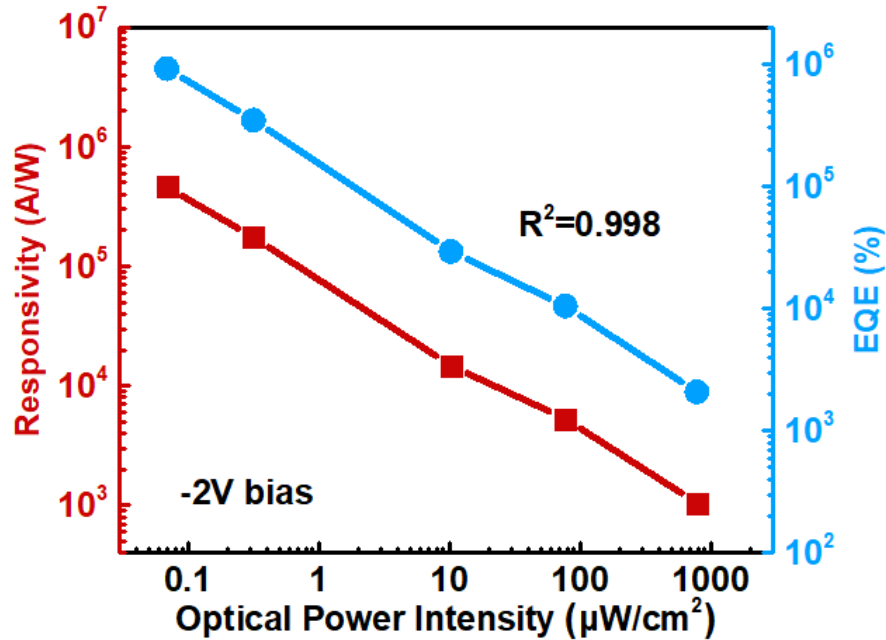
Figure 4.14 Power intensity dependence of Photoresponsivity and *EQE* under 0.433%

tensile strain.

Figure 4.15 indicates strong *R* and *EQE* under different strain and illumination conditions, which might be attributed to effective absorption and optimal device design. They also depict the dependency of *R* and *EQE* on the light power intensity irradiated on the device with application of multiple external strains. In photoconductivity photodetectors, the phenomena of decreasing responsivity as light intensity increases are common. With high-power light illumination, the quantity of photogenerated carriers accessible for extraction decreases due to the Auger process or recombination/trap states saturation, both of which affect the lifespan of the induced carriers.
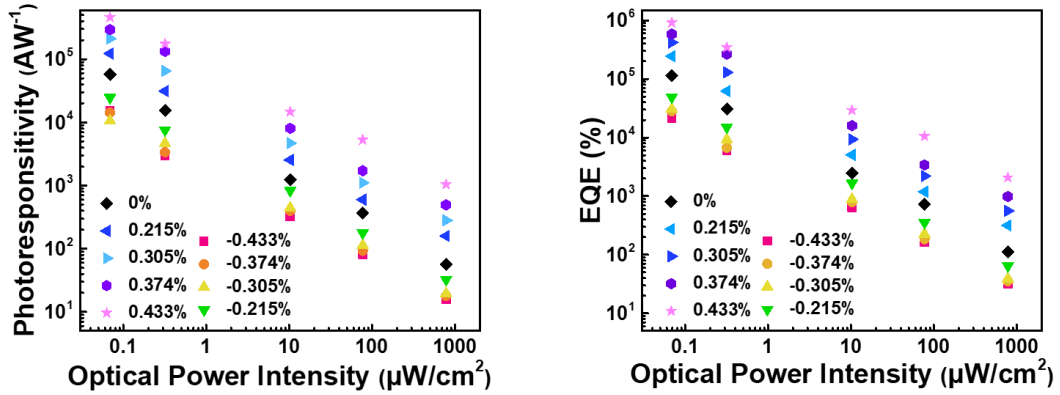
Figure 4.15 The optical power intensity dependence of photoresponsivity (left) and *EQE* (right) of the α-In₂Se₃/WSe₂ heterostructure photodetector at different strain conditions under -2 V bias.

For future practical applications, the independence of responsivity from incident light intensity is critical. Moreover, because the results were not acquired under the same conditions, a simple comparison of the photoresponsivity of photodetectors based on different vdW heterostructures might not be valid. As a result, *D** was obtained using the equation

$$D* = (A\Delta f)^{0.5} / NEP \qquad\qquad \text{Equation 5.3}$$

where *A* is the photodetector's effective area, f is the electrical bandwidth, and *NEP* is the noise equivalent power, displaced in Figure 4.16. Under each light illumination intensity, the *D** drops with applying compressive strain and raises with tensile strain, reaching a maximum value of 4.34×10^{14} Jones under weakest illumination of 0.069 μW/cm² and 0.433% tensile strain.

73
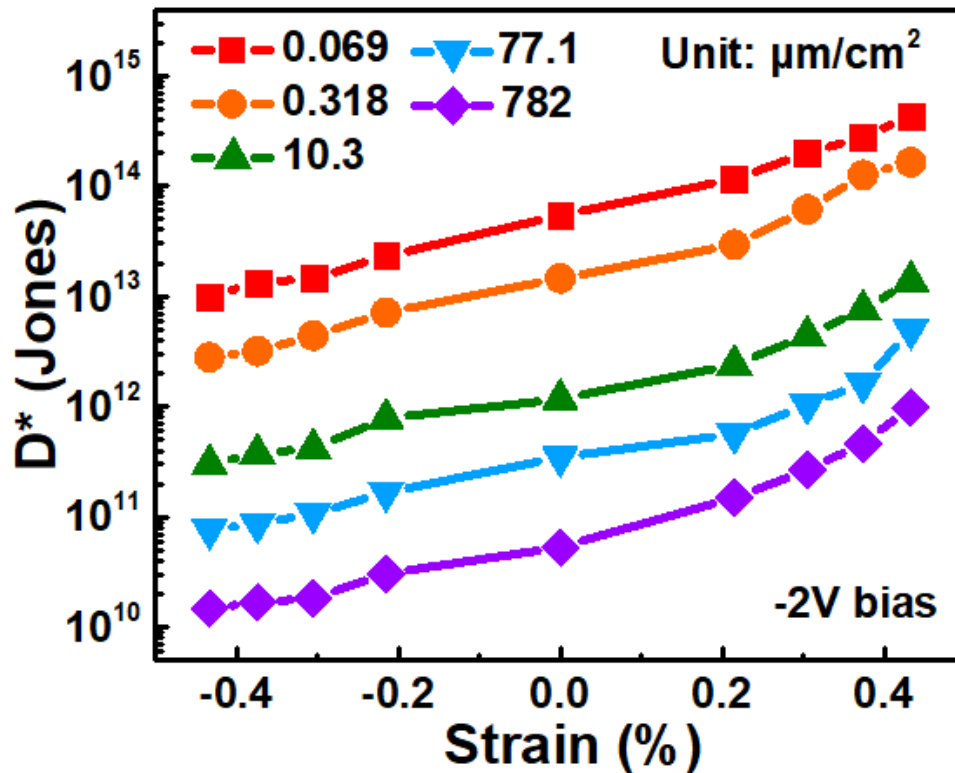
Figure 4.16 The strain dependence of D^* of the α-In$_2$Se$_3$/WSe$_2$ heterostructure

photodetector at different optical power intensity conditions under -2 V bias.

Under periodic on/off illumination, the device's photo-switching performance and time-dependent stability were also investigated. Without utilizing any external voltage bias, Figure 4.17 illustrates the detection of identifiable periodic switching photoresponse. Under 782 μW/cm^2 illumination and 0.433 % strain, each on and off state lasted about 100s and the device maintained the good photodetection stability for over 1000s condition. Each on/off switching takes less than 0.2 seconds to complete. The I_{ph} raises considerably

when light implies onto the photodetector, then rapidly reduces when the light source is switched off, and is strongly amplified by the tensile strain applied.
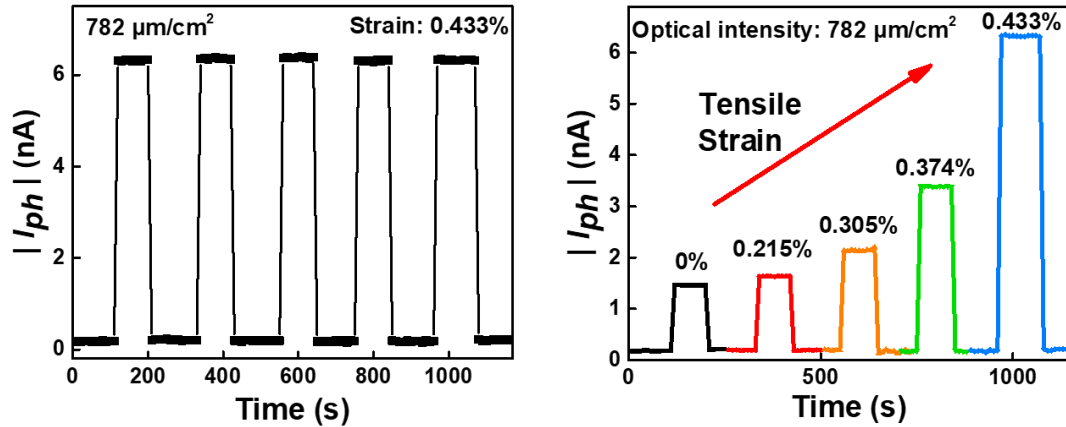
Figure 4.17 Temporal response of the $|I_{ph}|$ generation under periodic on/off light illumination tensile strain without external bias. (left) The $|I_{ph}|$ as a function of tensile strain under 782 μW/cm^2 light illumination without external bias. (right)

The previous study also investigated the influence of the piezo-phototronic effect on 2D-2D flexible van der Waals heterojunction photodetectors constructed with MoS$_2$ with odd atomic layers, as it is a piezoelectric semiconductor with good optoelectronic properties.[96] The device constructed with staking monolayer n-type MoS$_2$ and few-layer p-type WSe$_2$ was studied, where under -0.62% compressive strain condition, maximum values of the enhancement in photocurrent and respositivty are 86% and 3.4 mA/W, respectively. While higher intensity light (6.47 mW/cm^2) illuminates onto the photodiode, photocurrent increases 6.1% under tensile strain without turning point.[97] In comparison, our device performed much better under different strain and optical conditions, also the nanoflakes no longer limited by certain atomic layer to maintain piezoelectricity.

The modulation process of the piezo-phototronic effect on photodetector performance is further explained using schematic band diagrams of the heterostructure under various situations. The vdW heterojunction generated a foreseeable type-II band alignment based on the difference in bandgap and work function between α-In_2Se_3 and WSe_2, and the experimental outcomes demonstrate that the property is similar to that of diodes. Figure 4.18 depicts the offsets between the valence and conduction bands of an n-type α-In_2Se_3 and p-type WSe_2 heterojunction in the absence of light irradiation, mechanical strain, and voltage bias, which results in inducing the built-in electric field near the interface. When the n-type α-In_2Se_3 comes into contact with the p-type WSe_2, Fermi energy of two semiconductors adjust to the same level (shown in Figure 4.17).
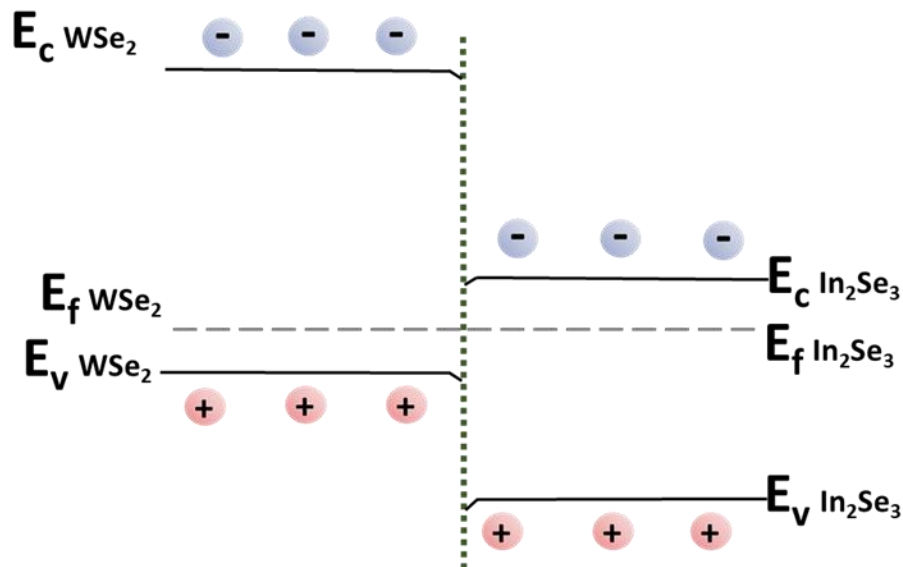
Figure 4.18 Schematic band structure diagram of α-In_2Se_3/WSe_2 heterojunction photodetector under strain-free and without light illumination condition.

As the penetration depth of incident light is greater than the thickness of the p-n junction, photons can be absorbed by both α-In$_2$Se$_3$ and WSe$_2$ when light illuminates onto the device (presented in Figure 4.19). Therefore, we suggested that the active region of the device is the area of nanoflakes inside the channel. The built-in potential dissociates free carriers from photo-generated electron-hole pairs and diffuses them through the depletion layer. External I_{ph} is formed when electrons and holes move towards α-In$_2$Se$_3$ and WSe$_2$ respectively. We believe that the I_{ph} observed in this study was mostly generated from the P-N heterojunction area since the separation capacity outside the P-N jointed region is weak.
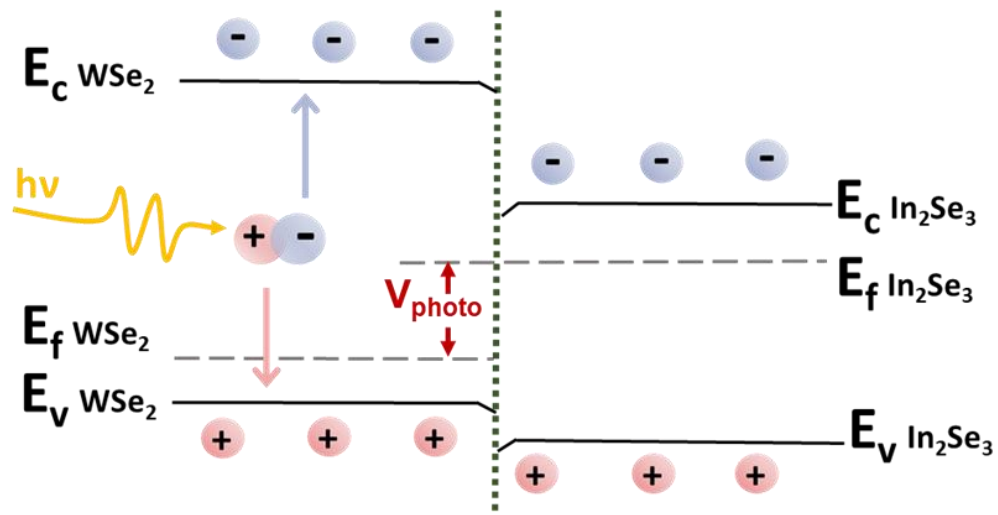
Figure 4.19 Schematic band structure diagram of α-In$_2$Se$_3$/WSe$_2$ heterojunction photodetector under strain-free and light illumination condition.

The conduction and valence energy bands are displayed in Figure 4.20 to investigate band structures under different strain conditions, with band structures under strain-free, tensile, and compressive strain represented by the black solid, red dash, and blue dash lines, respectively. Negative piezoelectric charges were induced at the boundary when tensile strain was applied, resulting in a higher band slope of α-In$_2$Se$_3$ at the heterojunction. The increased driving force for photo-generated electrons drifting from WSe$_2$ and α-In$_2$Se$_3$, at the interface due to the realignment of tilting energy bands improves the separation and transport efficiency of photo-induced excitons.
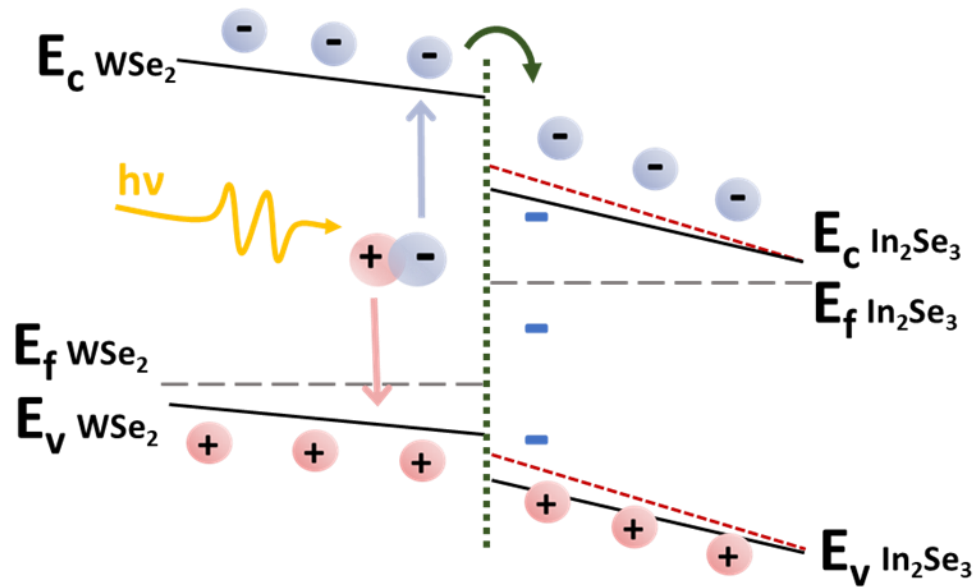
Figure 4.20 Schematic band structure diagram of α-In$_2$Se$_3$/WSe$_2$ heterojunction photodetector under tensile strain and light illumination condition.

Positive piezo-charges, on the other hand, are induced at α-In$_2$Se$_3$ when the photodetector is applied with compressive strain. The piezo-potential, as shown in Figure 4.21, gives the energy band of α-In$_2$Se$_3$ a gentler slope and increases the potential barrier at the junction, resulting in a reduction in driving force for photo-induced electrons to drift away from the α-In$_2$Se$_3$ side. As a result, the photo-excited carrier transport characteristic through the junction is restricted, and the photodetection performance is suppressed by the compressive strain.
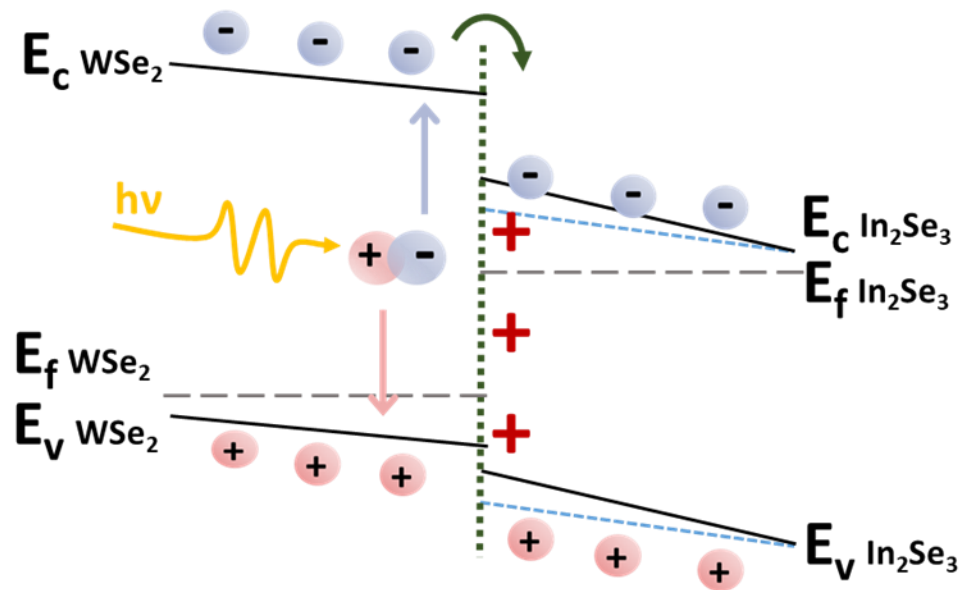
Figure 4.21 Schematic band structure diagram of α-In$_2$Se$_3$/WSe$_2$ heterojunction photodetector under compressive strain and light illumination condition.

The position of Fermi level relative to the valance band and conduction band remains the same during bending in semiconductors. The Fermi energy plotted in Figure 4c and 4d

ought to be tilted at the same tilting angle with the CB and VB. However, for simplicity and better illustration of the piezo-phototronic mechanism, we would like to focus the working mechanism on the effective strain tilting of CB and VB structure near the interface.

Because the P-N junction was constructed between the basal planes of the 2D-layered materials, both in-plane and out-of-plane polarizations could be regarded to contribute to the piezo-potential production on the interior of α-In$_2$Se$_3$. We believe that in-plane polarization preforms an important part in the carrier transportion along the lateral direction in the α-In$_2$Se$_3$ flake, whereas he out-of-plane polarization plays a critical role in the electron-hole separation near the depletion region of the p-n junction. When a photodetector is illuminated with high-intensity light, the carrier concentration of the 2D materials increases, resulting in a reduced density of effective piezoelectric polarization, commonly referred as the 'screen effect' of piezoelectric polarization charges. Thus, the photodetector's optical sensing performance changes significantly under various illumination situations.

4.4 Comparison of photodetector based on α-In$_2$Se$_3$ and α-In$_2$Se$_3$/WSe$_2$

With application of the mechanical strain, the induced piezoelectric charges can modulate the concentration and distribution of carriers at the vicinity of the Schottky barrier formed between metal contact and piezoelectric materials. In Hou's work, a flexible α-In$_2$Se$_3$-based transistor on a PET substrate with Au electrodes has been investigated with the optimized photoresponsivity increased by 200% with introducing external strain. They

attributed this elevated photoresponses to the modulation of carrier mobility and the local band profile tilting at the α-In$_2$Se$_3$-Au Schottky barrier contact caused by piezoelectric polarization charges.[38]

In this work, we also fabricated the flexible α-In$_2$Se$_3$/WSe$_2$ vdW P-N heterojunction device on PET substrate with Au electrodes. Based on the interaction between piezo-induced band tilting at the p-n junction and the Schottky barrier contact, the photoresponsivity of the flexible α-In$_2$Se$_3$/WSe$_2$ photodetector was significantly promoted up to about 1800% under 0.433% tensile strain, in stark contrast to the enhancement (~200%) in α-In$_2$Se$_3$-based photodetector which only contributed from the modulation of Schottky Barrier height in previous work. We believe that the contribution of P-N junction dominates over Schottky Barrier to the performance of our devices based on piezo-phototronic effect. We focus on demonstration of the piezo-phototronic mechanism near the α-In$_2$Se$_3$/WSe$_2$ p-n junction and developed excellent results.

Chapter 5 Conclusions and future prospect

5.1 Conclusion

Typical 2D materials are one of the hottest topic worldwide since discovered, as their ultra-thin planar structure and remarkable properties. They have significant mechanical properties in comparison to bulk materials. Besides, most of 2D materials have good ductility and transportation of electrons and holes, which are considered as suitable as materials for fabrication of photoelectronics with reduction in thickness. Recently, piezoelectric, piezotronic and piezo-phototronic effect of 2D materials are under highly research and development. With modulating potential due to stain-induced polarization, transportation behavior of mobile charge carriers and optoelectronic process can be enhanced, which is remarkable for design and production of phototronic and electronic devices. Heterostructures constructed with various materials have different controllable energy band structures that achieve notable electronic and optoelectronic characteristics different from uniformed single material. Moreover, heterojunctions or homostructures formed with different n-type or p-type 2D materials are also shown low dark current and fast time response that are suggestive materials for high performance photodetectors. In our work, performances of 2D heterstructure photodetectors are improved due to piezo-phototronic effect.

In conclusion, this thesis studies the influence of piezo-phototronic effect on a flexible α-In_2Se_3/WSe_2 vdW heterostructure and investigates the strain-modulated photodetection

performance of the heterostructure photodetector. The built-in potential at the p-n junction can promote the dissociation of photo-induced excitons into free carriers under LED illumination, driving electrons and holes to the α-In$_2$Se$_3$ and WSe$_2$ sides, respectively, resulting in a rise in photocurrent. By utilizing the strong piezoelectric effect in α-In$_2$Se$_3$, the photoresponse of the device can be further optimized by external mechanical strain. On account of piezo-phototronic effect, the strain-induced piezo-potential generated from the α-In$_2$Se$_3$ side can tune the band structure near the junction interface, allowing more efficient separation of photo-generated electron-hole pairs. The experimental results demonstrate that the output current can reach up to -164 nA under 0.433% strain and 782 μW/cm^2 optical intensity combining with the strain-induced piezo-potential, which is 304 times greater than dark current under strain-free condition. The maximum photoresponsivity and detectivity can reach up to 4.61×10^5 A/W and 4.34×10^{14} Jones under a low optical illumination power with 0.069 μW/cm^2 and 0.433% tensile strain. Our results suggest that the feasibility of vdW p-n heterostructures can be widely extended to other piezoelectric 2D materials, which may provide insights to develop high-performance flexible nano-optoelectronics.

5.2 Future prospectives

Nevertheless, there are still further progress in this field can be advanced. Firstly, devices based on 2D materials exist low production efficiency during film preparation and construction structures. Simple method what can be used to fabricate high-quality large-

scale 2D thin film will make the prospective applications in electrical devices more accessible.

Second, although there are many different types of 2D materials with varied optical and electrical properties, choosing the appropriate one for specific utilization is still a difficult part for designing a new device. We can discover more 2D piezoelectric materials, whose properties has been predicted based on theoretical calculations. As the 2D vdW heterostructure may generate new physical phenomena and build a variety of innovative devices, 2D materials serve as a foundation for the creation of heterostructures with various characteristics. The function and applications based on heterostructures can expand owing to the numerous 2D material combinations. Combining 2D piezoelectric materials with traditional 2D materials used to construct photodetectors will result in high performance optoelectronics. Also, other than piezoelectricity, there are many more characteristics such as pyroelectric, ferroelectric properties can be investigated, which can be beneficial to the multi-functionality of devices based on 2D materials.

Comparing to bulk materials, surface condition of 2D materials become significant through fabrication as they only consist of a single layer or few layer atoms. There are still many challenges need to be overcome before practical 2D materials applications can enter mass production stage.

References

[1]   S. Kim, K. Choi, B. Lee, Y. Kim, and B. Hong, "Materials for flexible, stretchable electronics: graphene and 2D materials," *Annu. Rev. Mater. Res.* **45**, 84, (2015).

[2]   K. Novoselov, A. Geim, S. Morozov, D. Jiang, Y. Zhang, S. Dubonos and A. Firsov, "Electric field in atomically thin carbon films," *Science* **306**, 666, (2004).

[3]   H. Conley, B. Wang, J. Ziegler, R. Haglund Jr, S. Pantelides, and K. Bolotin, "Bandgap engineering of strained monolayer and bilayer MoS2," *Nano Lett.* **13**, 3626, (2013).

[4]   D. Bandurin, A. Tyurnina, G. Yu, A. Mishchenko, V. Zólyomi, S. Morozov, R. Kumar, R. Gorbachev, Z. Kudrynskyi, S. Pezzini, Z. Kovalyuk, U. Zeitler, K. Novoselov, A. Patanè, L. Eaves, I. Grigorieva, V. Fal'ko, A. Geim and Y. Cao "High electron mobility, quantum Hall effect and anomalous optical response in atomically thin InSe," *Nat. Nanotechnol.* **12**, 223, (2017).

[5]   S. Yu, X. Wu, Y. Wang, X. Guo, and L. Tong, "2D Materials for Optical Modulation: Challenges and Opportunities," *Adv. Mater.* **29**, 1606128, (2017).

[6]   Z. Luo, J. Maassen, Y. Deng, Y. Du, R. Garrelts, M. Lundstrom, P. Ye and X. Xu, "Anisotropic in-plane thermal conductivity observed in few-layer black phosphorus," *Nat. Commun.* **6**, 1, (2015).

[7]   M. Al Mamun and M. Yuce, "Recent Progress in Nanomaterial Enabled Chemical

Sensors for Wearable Environmental Monitoring Applications," *Adv. Funct. Mater.* **30**, 2005703, (2020).

[8]   C. Tan, X. Cao, X. Wu, Q. He, J. Yang, X. Zhang, J. Chen, W. Zhao, S. Han, G. Nam, M. Sindoro and H. Zhang, "Recent Advances in Ultrathin Two-Dimensional Nanomaterials," *Chem. Rev.* **117**, 6225, (2017).

[9]   K. Novoselov, A. Mishchenko, A. Carvalho, and A. Neto, "2D materials and van der Waals heterostructures," *Science* **353**, aac9439, (2016).

[10]   D. Jariwala, T. Marks, and M. Hersam, "Mixed-dimensional van der Waals heterostructures," *Nat. Mater.* **16**, 170, (2017).

[11]   F. Schwierz, J. Pezoldt, and R. Granzner, "Two-dimensional materials and their prospects in transistor electronics," *Nanoscale* **7**, 8261, (2015).

[12]   Q. Wang, K. Kalantar-Zadeh, A. Kis, J. Coleman, and M. Strano, "Electronics and optoelectronics of two-dimensional transition metal dichalcogenides," *Nat. Nanotechnol.* **7**, 699, (2012).

[13]   P. Sahatiya and S. Badhulika, "Strain-modulation-assisted enhanced broadband photodetector based on large-area, flexible, few-layered Gr/MoS_2 on cellulose paper," *Nanotechnol.* **28**, 455204, (2017).

[14]   T. Dong, J. Simões, and Z. Yang, "Flexible photodetector based on 2D materials: processing, architectures, and applications," *Adv. Mater. Interfaces* **7**, 1901657, (2020).

[15]   E. Pomerantseva and Y. Gogotsi, "Two-dimensional heterostructures for energy

storage," *Nat. Energy* **2**, 1, (2017).

[16]   X. Wang, X. Lu, B. Liu, D. Chen, Y. Tong, and G. Shen, "Flexible energy-storage devices: design consideration and recent progress," *Adv. Mater.* 26, 4763, (2014).

[17]   G. Kakavelakis, E. Kymakis, and K. Petridis, "2D materials beyond graphene for metal halide perovskite solar cells," *Adv. Mater. Interfaces* **5**, 1800339, (2018).

[18]   Y. Zhang, Y. Yang, Y. Gu, X. Yan, Q. Liao, P. Li, Z. Zhang and Z. Wang "Performance and service behavior in 1-D nanostructured energy conversion devices," *Nano Energy* **14**, 30, (2015).

[19]   S. Yuan, S. Pang, and J. Hao, "2D transition metal dichalcogenides, carbides, nitrides, and their applications in supercapacitors and electrocatalytic hydrogen evolution reaction," *Appl. Phys. Rev.* **7**, 21304, (2020).

[20]   X. Zhang, X. Qiao, W. Shi, J. Wu, D. Jiang, and P. Tan, "Phonon and Raman scattering of two-dimensional transition metal dichalcogenides from monolayer, multilayer to bulk material," *Chem. Soc. Rev.* **44**, 2757, (2015).

[21]   B. Radisavljevic, A. Radenovic, J. Brivio, V. Giacometti, and A. Kis, "Single-layer MoS 2 transistors," *Nat. Nanotechnol.* **6**, 147, (2011).

[22]   Y. Ding, Y. Wang, J. Ni, L. Shi, S. Shi, and W. Tang, "First principles study of structural, vibrational and electronic properties of graphene-like MX_2 (M= Mo, Nb, W, Ta; X= S, Se, Te) monolayers," *Phys. B Condens. Matter* **406**, 2254, (2011).

[23]   Z. Wang, Q. Su, G. Yin, J. Shi, H. Deng, J. Guan, M. Wu, Y. Zhou, H. Lou and Y.Fu, "Structure and electronic properties of transition metal dichalcogenide MX_2 (M= Mo, W, Nb; X= S, Se) monolayers with grain boundaries," *Mater. Chem. Phys.* **147**, 1068, (2014).

[24]   C. Ataca, H. Sahin, and S. Ciraci, "Stable, single-layer MX_2 transition-metal oxides and dichalcogenides in a honeycomb-like structure," *J. Phys. Chem. C* **116**, 8983, (2012).

[25]   L. Mattheiss, "Band structures of transition-metal-dichalcogenide layer compounds," *Phys. Rev. B* **8**, 3719, (1973).

[26]   M. Chhowalla, Z. Liu, and H. Zhang, "Two-dimensional transition metal dichalcogenide (TMD) nanosheets," *Chem. Soc. Rev.* **44**, 2584, (2015).

[27]   M. Chhowalla, H. Shin, G. Eda, L. Li, K. Loh, and H. Zhang, "The chemistry of two-dimensional layered transition metal dichalcogenide nanosheets," *Nat. Chem.* **5**, 263, (2013).

[28]   M. Springford, "The luminescence characteristics of some group III-VI compounds," *Proc. Phys. Soc.* **82**, 1020, (1963).

[29]   D. Lee, T. Kim, and H. Sohn, "Highly reliable threshold switching behavior of amorphous Ga_2Te_3 films deposited by RF sputtering," *Appl. Phys. Express* **12**, 85504, (2019).

[30]   K. George, C. Groot, C. Gurnani, A. Hector, R. Huang, M. Jura, W. Levason, and G. Reid, "Telluroether and selenoether complexes as single source reagents for

low pressure chemical vapor deposition of crystalline Ga_2Te_3 and Ga_2Se_3 thin films," *Chem. Mater.* **25**, 1829, (2013).

[31]   A. Bekheet, "Electrical and optical properties of amorphous Ga_2Te_3 films," *Eur. Phys. Journal-Applied Phys.* **16**, 187, (2001).

[32]   V. Sowjanya, K. Bangera, and G. Shivakumar, "Structural, electrical and optical properties of stoichiometric In_2Te_3 thin films," *Ceram. Int.* **43**, 3748, (2017).

[33]   J. Yao, Z. Deng, Z. Zheng, and G. Yang, "Stable, fast UV–Vis–NIR photodetector with excellent responsivity, detectivity, and sensitivity based on α-In_2Te_3 films with a direct bandgap," *ACS Appl. Mater. Interfaces* **8**, 20872, (2016).

[34]   T. Zhai, X. Fang, M. Liao, X. Xu, L. Li, B. Liu, Y. Koide, Y. Ma, J. Yao, Y. Bando, and D. Golberg, "Fabrication of high-quality In_2Se_3 nanowire arrays toward high-performance visible-light photodetectors," *ACS Nano* **4**, 1596, (2010).

[35]   Z. Zheng, J. Yao, J. Xiao, and G. Yang, "Synergistic effect of hybrid multilayer In_2Se_3 and nanodiamonds for highly sensitive photodetectors," *ACS Appl. Mater. Interfaces* **8**, 20200, (2016).

[36]   F. Guo, Y. Lyu, M. Jedrzejczyk, Y. Zhao, W. Io, G. Bai, W. Wu, and J. Hao, "Piezoelectric biaxial strain effects on the optical and photoluminescence spectra of 2D III–VI compound α-In_2Se_3 nanosheets," *Appl. Phys. Lett.* **116**, 113101, (2020).

[37]   M. Küpers, P. Konze, A. Meledin, J. Mayer, U. Englert, M. Wuttig and R. Dronskowski, "Controlled crystal growth of indium selenide, In2Se3, and the crystal structures of α-In$_2$Se$_3$," *Inorg. Chem.* **57**, 11775, (2018).

[38]   P. Hou, Y. Lv, Y. Chen, Y. Liu, C. Wang, P. Zhou, X. Zhong, J. Wang, and X. Ouyang, "In-Plane Strain-Modulated Photoresponsivity of the α-In$_2$Se$_3$-Based Flexible Transistor," *ACS Appl. Electron. Mater.* **2**, 140, (2019).

[39]   V. Kaminskii, Z. Kovalyuk, A. Zaslonkin, and V. Ivanov, "Structure and electrical properties of In$_2$Se$_3$Mn layered crystals," *Semicond. Phys. Quantum Electron. Optoelectron.* **12**, 290, (2009).

[40]   V. Kaminskii, Z. Kovalyuk, A. Zaslonkin, and V. Ivanov, "Electrical properties of In$_2$Se$_3$<Mn> and InSe< Mn> crystals," *Inorg. Mater.* **48**, 103, (2012).

[41]   A. Zaslonkin, Z. Kovalyuk, and I. Mintyanskii, "Electrical properties of In$_2$Se$_3$ layered crystals doped with cadmium, iodine, or copper," *Inorg. Mater.* **43**, 1271, (2007).

[42]   H. Peng, C. Xie, D. Schoen, and Y. Cui, "Large anisotropy of electrical properties in layer-structured In$_2$Se$_3$ nanowires," *Nano Lett.* **8**, 1511, (2008).

[43]   C. Zheng, L. Yu, L. Zhu, J. Collins, D. Kim, Y. Lou, C. Xu, M. Li, Z. Wei, Y. Zhang, M. Edmonds, S. Li, J. Seidel, Y. Zhu, J. Liu, W. Tang and M. Fuhrer "Room temperature in-plane ferroelectricity in van der Waals In$_2$Se$_3$," *Sci. Adv.* **4**, eaar7720, (2018).

[44]   F. Xue, W. Hu, K. Lee, L. Lu, J. Zhang, H. Tang, A. Han, W. Hsu, S. Tu, W.

Chang, C. Lien, J. He, Z. Zhang, L. Li and X. Zhang, "Room-temperature ferroelectricity in hexagonally layered α-In$_2$Se$_3$ nanoflakes down to the monolayer limit," *Adv. Funct. Mater.* **28**, 1803738, (2018).

[45]   F. Ohuchi, B. Parkinson, K. Ueno, and A. Koma, "van der Waals epitaxial growth and characterization of MoSe$_2$ thin films on SnS$_2$," *J. Appl. Phys.* **68**, 2168, (1990).

[46]   X. Li, L. Basile, B. Huang, C. Ma, J. Lee, I. Vlassiouk, A. Puretzky, M. Lin, M. Yoon, M. Chi, J. Idrobo, C. Rouleau, B. Sumpter, D. Geohegan, and K. Xiao "Van der Waals epitaxial growth of two-dimensional single-crystalline GaSe domains on graphene," *ACS Nano* **9**, 8078, (2015).

[47]   A. Yan, J. Velasco, Jr., S. Kahn, K. Watanabe, T. Taniguchi, F. Wang, M. Crommie, and A. Zettl "Direct growth of single-and few-layer MoS$_2$ on h-BN with preferred relative rotation angles," *Nano Lett.* **15**, 6324, (2015).

[48]   M. Cattelan, B. Markman, G. Lucchini, P. Das, I. Vobornik, J. Robinson, S. Agnoli, and G. Granozzi "New strategy for the growth of complex heterostructures based on different 2D materials," *Chem. Mater.* **27**, 4105, (2015).

[49]   E. Xenogiannopoulou *et al.*, P. Tsipas, K. Aretouli, D. Tsoutsou, S. Giamini, C. Bazioti, G. Dimitrakopulos, P. Komninou, S. Brems, C. Huyghebaert, I. Radu, A. Dimoulas "High-quality, large-area MoSe$_2$ and MoSe$_2$/Bi$_2$Se$_3$ heterostructures on AlN (0001)/Si (111) substrates by molecular beam epitaxy," *Nanoscale* **7**, 7896, (2015).

[50]   Z. Huang, J. Carey, M. Liu, X. Guo, E. Mazur, and J. Campbell, "Microstructured silicon photodetector," *Appl. Phys. Lett.* **89**, 33506, (2006).

[51]   N. Huo and G. Konstantatos, "Recent progress and future prospects of 2D-based photodetectors," *Adv. Mater.* **30**, 1801164, (2018).

[52]   T. Han, H. Ruan, S. Cao, Y. Guan, D. Tang, and X. Yang, *Photoelectric Materials and Devices*. World Scientific, (2021).

[53]   F. Xia, T. Mueller, Y. Lin, A. Valdes-Garcia, and P. Avouris, "Ultrafast graphene photodetector," *Nat. Nanotechnol.* **4**, 839, (2009).

[54]   K. Novoselov, V. Fal, L. Colombo, P. Gellert, M. Schwab and K. Kim, "A roadmap for graphene," *Nature* **490**, 192, (2012).

[55]   R. Wang, X. Ren, Z. Yan, L. Jiang, E. Wei, and G. Shan, "Graphene based functional devices: A short review," *Front. Phys.* **14**, 13603, (2019).

[56]   A. Castro Neto, F. Guinea, N. Peres, K. Novoselov, and A. Geim, "The electronic properties of graphene," *Rev. Mod. Phys.* **81**, 109, (2009).

[57]   T. Mueller, F. Xia, and P. Avouris, "Graphene photodetectors for high-speed optical communications," *Nat. Photonics* **4**, 297, (2010).

[58]   I. Omkaram, Y. Hong, and S. Kim, "Transition metal dichalcogenide photodetectors," *Two-Dimensional Mater. Photodetector*, 2018.

[59]   D. Kang, S. Pae, J. Shim, G. Yoo, J. Jeon, J. Leem, J. Yu, S. Lee, B. Shin, J. Park "An ultrahigh-performance photodetector based on a perovskite–transition-metal-

dichalcogenide hybrid structure," *Adv. Mater.* 28, 7799, (2016).

[60] O. Lopez-Sanchez, D. Lembke, M. Kayci, A. Radenovic, and A. Kis, "Ultrasensitive photodetectors based on monolayer MoS_2," *Nat. Nanotechnol.* **8**, 497, (2013).

[61] M. Long, P. Wang, H. Fang, and W. Hu, "Progress, challenges, and opportunities for 2D material based photodetectors," *Adv. Funct. Mater.* **29**, 1803807, (2019).

[62] W. Tian, H. Sun, L. Chen, P. Wangyang, X. Chen, J. Xiong, L. Li "Low-dimensional nanomaterial/Si heterostructure-based photodetectors," *InfoMat* **2**, 140, (2019).

[63] Z. Wang, R. Yu, X. Wen, Y. Liu, C. Pan, W. Wu, and Z. Wang "Optimizing performance of silicon-based p–n junction photodetectors by the piezo-phototronic effect," *ACS Nano* **8**, 12866, (2014).

[64] B. Peng, G. Yu, X. Liu, B. Liu, X. Liang, L. Bi, L. Deng, T. Sum and K. Loh, "Ultrafast charge transfer in MoS_2/WSe_2 p–n Heterojunction," *2D Mater.* **3**, 25020, (2016).

[65] K. Zhang, M. Peng, W. Wu, J. Guo, G. Gao, Y. Liu, J. Kou, R. Wen, Y. Lei, A. Yu, Y. Zhang, J. Zhai and Z. Wang "A flexible p-CuO/n-MoS_2 heterojunction photodetector with enhanced photoresponse by the piezo-phototronic effect," *Mater. Horizons* **4**, 274, (2017).

[66] S. Yuan, W. Io, J. Mao, Y. Chen, X. Luo, and J. Hao, "Enhanced Piezoelectric Response of Layered In_2Se_3/MoS_2 Nanosheet-Based van der Waals

Heterostructures," *ACS Appl. Nano Mater.* **3**, 11979, (2020).

[67] K. Michel and B. Verberck, "Theory of elastic and piezoelectric effects in two-dimensional hexagonal boron nitride," *Phys. Rev. B* **80**, 224301, (2009).

[68] Y. Zhang, W. Jie, P. Chen, W. Liu, and J. Hao, "Ferroelectric and piezoelectric effects on the optical process in advanced materials and devices," *Adv. Mater.* **30**, 1707007, (2018).

[69] K. Michel and B. Verberck, "Phonon dispersions and piezoelectricity in bulk and multilayers of hexagonal boron nitride," *Phys. Rev. B* **83**, 115328, (2011).

[70] J. Song, J. Zhou, and Z. Wang, "Piezoelectric and semiconducting coupled power generating process of a single ZnO belt/wire. A technology for harvesting electricity from the environment," *Nano Lett.* **6**, 1656, (2006).

[71] N. Soin, S. Anand, and T. Shah, "Energy harvesting and storage textiles," in *Handbook of Technical Textiles*, Elsevier, 357, (2016).

[72] Z. Wang, "Towards self-powered nanosystems: from nanogenerators to nanopiezotronics," *Adv. Funct. Mater.* **18**, 3553, (2008).

[73] M. Gupta and S. Suman, "Electricity generation due to vibration of moving vehicles using piezoelectric effect," *Adv. Electron. Electr. Eng* **4**, (2014).

[74] J. Lee *et al.*, J. Park, E. Cho, T. Kim, S. Han, T. Kim, Y. Liu, S. Kim, C. Roh, H. Yoon, H. Ryu, W. Seung, J. Lee, J. Lee, S. Kim "Reliable piezoelectricity in bilayer WSe_2 for piezoelectric nanogenerators," *Adv. Mater.* **29**, 1606667, (2017).

[75]   Y. Hu, Y. Chang, P. Fei, R. Snyder, and Z. Wang, "Designing the electric transport characteristics of ZnO micro/nanowire devices by coupling piezoelectric and photoexcitation effects," *ACS Nano* **4**, 1234, 2010.

[76]   Y. Liu, Q. Yang, Y. Zhang, Z. Yang, and Z. Wang, "Nanowire piezo-phototronic photodetector: theory and experimental design," *Adv. Mater.* **24**, 1410, (2012).

[77]   C. Pan, M. Chen, R. Yu, Q. Yang, Y. Hu, Y. Zhang and Z. Wang, "Progress in Piezo-Phototronic-Effect-Enhanced Light-Emitting Diodes and Pressure Imaging," *Adv. Mater.* **28**, 1535, (2016).

[78]   Z. L. Wang, *Piezotronics and Piezo-phototronics*. Springer Science & Business Media, (2013).

[79]   F. Xue, J. Zhang, W. Hu, W. Hsu, A. Han, S. Leung, J. Huang, Y. Wan, S. Liu, J. Zhang, J. He, W. Chang, Z. Wang, X. Zhang and L. Li "Multidirection piezoelectricity in mono-and multilayered hexagonal α-In$_2$Se$_3$," *ACS Nano* **12**, 4976, (2018).

[80]   E. Rhoderick, "Metal-semiconductor contacts," *IEE Proc. I-Solid-State Electron Devices* **129**, 1, (1982).

[81]   M. Que, X. Wang, Y. Peng, and C. Pan, "Flexible electrically pumped random lasing from ZnO nanowires based on metal–insulator–semiconductor structure," *Chinese Phys. B* **26**, 67301, (2017).

[82]   L. Brillson and Y. Lu, "ZnO Schottky barriers and Ohmic contacts," *J. Appl. Phys.* **109**, 8, (2011).

[83] M. Dai, H. Chen, F. Wang, Y. Hu, S. Wei, J. Zhang, Z. Wang, T. Zhai, and P. Hu "Robust Piezo-Phototronic Effect in Multilayer γ-InSe for High-Performance Self-Powered Flexible Photodetectors," *ACS Nano* **13**, 7291, (2019).

[84] C. Dervos, P. Skafidas, J. Mergos, and P. Vassiliou, "pn junction photocurrent modelling evaluation under optical and electrical excitation," *Sensors* **4**, 58, (2004).

[85] X. Yu, Y. Shen, T. Liu, T. Wu, and Q. Wang, "Photocurrent generation in lateral graphene pn junction created by electron-beam irradiation," *Sci. Rep.* **5**, 1, (2015).

[86] E. Enlow and D. Alexander, "Photocurrent modeling of modern microcircuit pn junctions," *IEEE Trans. Nucl. Sci.* 35, 1467, (1988).

[87] S. Dhariwal, L. Kothari, and S. Jain, "Saturation of photovoltage and photocurrent in pn junction solar cells," *IEEE Trans. Electron Devices* **23**, 504, (1976).

[88] K. Novoselov and A. Neto, "Two-dimensional crystals-based heterostructures: materials with tailored properties," *Phys. Scr.* **2012**, 14006, (2012).

[89] S. Nasir, M. Hussein, Z. Zainal, N. Yusof, S. Zobir, and I. Alibe, "Potential valorization of by-product materials from oil palm: A review of alternative and sustainable carbon sources for carbon-based nanomaterials synthesis," *BioResources* **14**, 2352, (2019).

[90] K. Ember, M. Hoeve, S. McAughtrie, M. Bergholt, B. Dwyer, M Stevens, K. Faulds, S. Forbes and C. Campbell "Raman spectroscopy and regenerative medicine: a review," *NPJ Regen. Med.* **2**, 1, (2017).

[91] F. Ruggeri, J. Habchi, A. Cerreta, and G. Dietler, "AFM-based single molecule techniques: unraveling the amyloid pathogenic species," *Curr. Pharm. Des.* **22**, 3950, (2016).

[92] R. Gurwitz, R. Cohen, and I. Shalish, "Interaction of light with the ZnO surface: Photon induced oxygen 'breathing,' oxygen vacancies, persistent photoconductivity, and persistent photovoltage," *J. Appl. Phys.* **115**, 33701, (2014).

[93] Y. Zhao, F. Guo, R. Ding, W. Io, S. Pang, W. Wu and J. Hao "Piezo-Phototronic Effect in 2D α-In$_2$Se$_3$/WSe$_2$ van der Waals Heterostructure for Photodetector with Enhanced Photoresponse," *Adv. Opt. Mater.* **9**, 2100864, (2021).

[94] S. K. Kim, R. Bhatia, T. Kim, D. Seol, J. Kim, H. Kim, W. Seung, Y. Kim, Y. Lee and S. Kim"Directional dependent piezoelectric effect in CVD grown monolayer MoS$_2$ for flexible piezoelectric nanogenerators," *Nano Energy* **22**, 483, (2016).

[95] H. Fang and W. Hu, "Photogating in low dimensional photodetectors," *Adv. Sci.* **4**, 1700323, (2017).

[96] W. Wu, L. Wang, Y. Li, F. Zhang, L. Lin, S. Niu, D. Chenet, X. Zhang, Y. Hao, T. Heinz, J. Hone and Z. Wang "Piezoelectricity of single-atomic-layer MoS$_2$ for energy conversion and piezotronics," *Nature* **514**, 470, (2014).

[97] P. Lin, L. Zhu, D. Li, L. Xu, C. Pan, and Z. Wang, "Piezo-phototronic effect for enhanced flexible MoS$_2$/WSe$_2$ van der Waals photodiodes," *Adv. Funct. Mater.*

28, 1802849, (2018).